Multifield nested metafilters for wave propagation control

Francesca Fantoni [a], Emanuela Bosco [b,*], Andrea Bacigalupo [c]

[a] Department of Civil, Environmental, Architectural Engineering and Mathematics, University of Brescia, Brescia, Italy
[b] Department of the Built Environment, Eindhoven University of Technology, Eindhoven, The Netherlands
[c] Department of Civil, Chemical and Environmental Engineering, University of Genoa, Genoa, Italy

ARTICLE INFO

ABSTRACT

The present work proposes a novel class of multifield nested tunable metadevices that serve as high performance acoustic metafilters. The designed metafilter is characterized by a multiscale, hierarchical structure. At the mesoscale, the metamaterial consists of a sequence of two different periodically alternating layers: a polymeric homogeneous layer, which exhibits a viscoelastic constitutive response, and a microstructured one. The latter is based on the periodic repetition of a multiphase microscale cell that is composed by a stiff elastic external coating, a viscoelastic phase and an internal disk of piezoelectric material shunted by an external electrical circuit having a tunable impedance/admittance This tuning parameter affects the constitutive elastic properties of the piezoelectric phase and, in turn, the overall response of the microscale cell, thereby ultimately enabling to achieve an optimal filtering performance for the metadevice. Due to the periodicity of the multiphase cell at the microscale, a two-scale variational-asymptotic homogenization technique is exploited in the frequency domain in order to obtain the frequency-dependent overall constitutive properties of the microstructured layer. Subsequently, in-plane free wave propagation inside the periodic multilayered metamaterial at the mesoscale is investigated by means of Floquet–Bloch theory, together with the transfer matrix method. By triggering the shunting effect, a stiffening of the piezoelectric phase can be achieved, which is demonstrated to open low frequency band gaps in the metamaterial frequency spectrum. The filtering capability of the metadevice has been assessed as a function of its geometrical features and the tuning parameter, thus paving the way towards the design of sophisticated and topologically optimized acoustic filters.

© 2022 The Author(s). Published by Elsevier Ltd. This is an open access article under the CC BY license (http://creativecommons.org/licenses/by/4.0/).

1. Introduction

Metamaterials are a class of composite materials that are artificially designed to exhibit extraordinary wave manipulation properties, for which the effective material constitutive response substantially exceeds that of classical materials. The exotic properties of metamaterials enable to exploit them in several relevant engineering applications, which include acoustic filtering [1–4], wave guiding and polarization [5–8], self-collimation [9–11], energy transfer, harvesting, and sensing [12–18] and passive band gap control [19–25]. In order to target the desired effective response, metamaterials may be in general architected by tailoring their geometry and composing phases to achieve specific mechanical properties, such as mass density, inertia and stiffness [26–31]. Alternatively, when focusing in particular on acoustic metamaterials, the design may depart from a periodic lattice material or from a periodic microstructure consisting of a matrix with embedded inclusions, to which inertial or Helmholtz spatially-local resonators are added [32–42]. These local resonators allow to generate a strong coupling to the propagating wave in the sub-wavelength regime, whereby the wavelength is much larger than the characteristic size of the microstructure, while the frequency approximates the natural frequency of the resonators. These features enable to circumvent typical limitations of standard materials, thereby offering the possibility to exploit phenomena as negative refraction [17,43–45], invisibility of defects embedded into lattice and continuous systems [27,46, 47], and to overcome the diffraction limit [48,49].

In recent years, acoustic metamaterials composed of *active* phases have received growing research interest, as discussed in the comprehensive review presented in [50]. The use of active elements, such as e.g. piezoelectric, piezomagnetic, and magnetostrictive materials, particularly allows to take advantage of the intrinsic couplings between mechanical deformation and electric or magnetic fields, which opens new opportunities in physical and technical applications. In this context, in piezoelectric acoustic metamaterials, the mechanical and the electrical fields are coupled by means of piezoelectric patches shunted by electrical networks, generally referred to as *shunted piezoelectric phases*.

* Corresponding author.
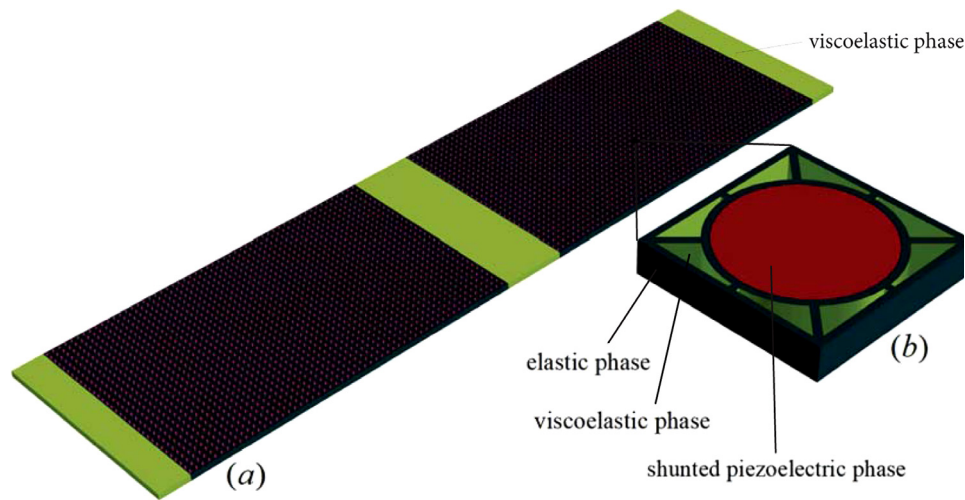 *E-mail address:* e.bosco@tue.nl (E. Bosco).

Fig. 1. Three-dimensional view of the proposed multiscale shunted piezoelectric acoustic metafilter. (a) Generic portion of the multilayer domain, which is infinitely extended along two perpendicular directions and consists of two different alternating layers: a homogeneous polymeric viscoelastic layer (yellow color) and a microstructured layer. (b) Detail of the multiphase cell composing the microstructured layer, which comprises a rigid phase (gray color), a polymeric viscoelastic phase (yellow color) and a shunted piezoelectric core (red color).

Accordingly, the effective response of the metamaterial can be tuned to control its dynamic effective density [51], bulk modulus [52], or both material properties [53], which is typically achieved by integrating piezoelectric elements into Helmholtz resonator systems. This enables shunted piezoelectric metamaterials to reveal extraordinary acoustic and mechanical properties that can be applied in noise, vibration and wave propagation control technologies [54–57].

In this paper, a tunable multiscale piezoelectric metadevice is designed with the aim of obtaining an exceptional filtering performance. The metamaterial is based on a multilayer hierarchical structure consisting of two different periodically alternating layers, as illustrated in Fig. 1. The first layer, which is indicated by the yellow color in Fig. 1(a), is made of a homogeneous polymeric material characterized by a viscoelastic constitutive response. The second layer consists of a heterogeneous microstructured material that is obtained by the periodic in-plane repetition of a multiphase cell, depicted in Fig. 1(b), which contains a piezoelectric phase shunted by an electrical circuit. In detail, the multiphase cell is characterized by a heavy, elastic stiff structure consisting of an external coating connected to an internal ring by means of connecting elements, as identified by the gray colored domain in Fig. 1(b). The regions located between the coating and the ring are made of a viscoelastic polymeric material, while the internal disk is composed by the shunted piezoelectric material connected to the electrical circuit. These two phases are respectively denoted by the yellow and the red colors in Fig. 1(b). By exploiting the piezoelectric coupling, a variation in the equivalent impedance/admittance of the electrical circuit enables to tune the constitutive properties of the shunting piezoelectric phase. Consequently, the overall constitutive response of the multiphase cell, and further of the entire multiscale metamaterial, can be fully tailored as a function of the parameters of the electrical circuit, without the need of modifying the microstructural geometry and/or the material properties of the non-shunted components.

In this setting, the effective mechanical properties of the microstructured layer are first derived by means of asymptotic homogenization [58,59]. Asymptotic homogenization applies to heterogeneous domains characterized by an underlying periodic microscale structure. This multiscale framework allows to represent the heterogeneous medium with rapidly oscillating material properties as an equivalent homogeneous domain, whereby the effective material response is obtained from the microscale fields through an averaging procedure based on rigorous mathematical principles. The method departs from writing the displacement field as an asymptotic expansion, and next inserting it into the equilibrium equation. This leads to the definition of boundary value problems defined on the microstructural domain (the so-called *cell problems*), which are typically resolved numerically by means of finite elements, for specific geometries of the microscale cell. From the solution of the cell problems, the effective material properties are obtained, together with the local microstructural displacement, strain and stress fields. The method is thus appealing for a broad range of applications, including thermo-mechanical [60–62], thermo-diffusive [63] and elasto-diffusive [64], thermo-piezoelectric [65–67], hygro-mechanical [68–70], and chemo-diffusive-mechanical [71] problems. By applying a bilateral Laplace transform in time [72] to governing equations at the microscale, the effective response of the microstructured layer considered in this communication will be determined as a function of the tuning parameter of the piezoelectric phase, while simultaneously accounting for the frequency-dependency of the properties of the viscoelastic constituent. Further, once the effective response of the microstructured material is known, the multilayered structure at the mesoscale will be treated as if each layer is homogeneous.

This enables to investigate dispersive free wave propagation within the multilayer domain. By further adopting a Floquet–Bloch decomposition [73] of the transformed displacement field and by means of a generalization of the transfer matrix method [74,75], an eigenproblem is obtained that allows to investigate propagation and spatial damping of Bloch waves in the metafilter. From this, the complex frequency spectrum of the first-order equivalent multilayered medium is derived, thereby demonstrating that, as a function of the tuned response of the piezoelectric phase, high performance wave control can be achieved.

This paper is organized as follows. In Section 2, the multiscale geometry of the proposed tunable piezoelectric acoustic metadevice is described, followed by the constitutive characterization of the piezoelectric and viscoelastic phases. Section 3 presents a review of the asymptotic homogenization framework, by defining the governing field equations at the microscale, the asymptotic expansion of the displacement field, the cell problems and the effective constitutive properties. The derivation of the complex frequency spectrum of the equivalent macroscopic domain is next

outlined in Section 4. The performance of the piezoelectric acoustic metamaterial is demonstrated in Section 5, which presents the tunable frequency-dependent effective and local mechanical response of the multiphase cell and the complex frequency spectrum of the effective medium. Finally, the main conclusions of the study are summarized in Section 6.

2. Multiscale metamaterial description

The proposed metamaterial is characterized by a multiscale and multiphase structure, which is described in detail in Section 2.1. The constitutive characterization of the material phases composing the metadevice is further presented in Section 2.2.

2.1. Multiscale geometry of the metamaterial

Consider the multilayer hierarchical metamaterial, unlimited in plane, which is sketched in Fig. 1(a). It is made of a stack of two different types of layers, which are periodically repeated along one in-plane direction and are characterized by the same thickness w in the out-of-plane direction. Perfect kinematic compatibility (i.e., perfect bonding) at the interface between the two layers is assumed to hold. One of the layers (indicated by the yellow color in Fig. 1(a)) is composed of a homogeneous polymeric material. The second layer is a heterogeneous microstructured layer, which is obtained by spanning a multiphase cell $\mathcal{A}_m$ along two perpendicular in-plane directions. The microscopic periodic cell $\mathcal{A}_m$, which is depicted in Fig. 1(b), is composed of an external stiffening coating of thickness d that is connected to an internal ring of mean radius R, by means of eight connecting elements. Both the internal ring and the connecting elements are characterized by the same thickness d. The coating, the connections and the internal ring are all made of steel (indicated by the gray color in Fig. 1(b)). The region between the external coating and the internal ring is occupied by the same polymeric material constituting the homogeneous layer and it is identified by a yellow color in Fig. 1(b). The internal disk of the periodic cell $\mathcal{A}_m$ (depicted with red color in Fig. 1(b)), has a radius equal to r, and is made by a piezoelectric material, which is separated from the steel phase by a thin dielectric insulator interface. As proved in the following, the described hierarchical multilayer metamaterial can be tuned in order to design high performance filters.

The intrinsically multiscale structure of the proposed metamaterial allows the identification of three different characteristic length scales: the structural or macroscopic one ℓ_S, the mesoscopic one ℓ_M, and the microstructural one ℓ_m. As depicted in Fig. 2, the hierarchical material can be described from a two-dimensional perspective, where vector $\mathbf{x} = x_1\mathbf{e}_1 + x_2\mathbf{e}_2$ identifies the position vector of each material point in a Cartesian coordinate system $\{\mathbf{e}_1, \mathbf{e}_2\}$. The multilayer structure is suitably characterized at the macrostructural level. At the mesoscale, a domain $\mathcal{C}_M = [0, L] \times [0, \delta L_2]$ is defined, where $L = L_1 + L_2$ with L_1 and L_2 the lengths of the homogeneous and microstructured layer, respectively, along direction $\mathbf{e}_2$ perpendicular to the layering, and $\delta \in \mathbb{R}^+$. Within domain $\mathcal{C}_M$, a cluster of microcells $\mathcal{L} = [0, L_2] \times [0, \delta L_2]$ is identified, which can be considered as a true representative portion of the microstructured material. From this representation, a periodic cell of the microstructured system $\mathcal{B}_m = [0, L] \times [0, \varepsilon]$ is recognized, whereby ε is the size of the microscopic cell $\mathcal{A}_m$ along both $\mathbf{e}_1$ and $\mathbf{e}_2$. Because of scale separation requirements, conditions $L_2 \gg \varepsilon$ and $\delta L_2 \gg \varepsilon$ must hold. The micro periodic cell $\mathcal{A}_m$, which is properly described at the microscale, is characterized by two periodicity vectors $\mathbf{v}_1 = \varepsilon\mathbf{e}_1$ and $\mathbf{v}_2 = \varepsilon\mathbf{e}_2$. In this scenario, homogenization techniques can be wisely exploited in order to describe material behavior in a concise and, at the same time, accurate way, by properly

taking into account the effects of heterogeneities upon the global system response. In particular, a two-scale variational-asymptotic homogenization method is here employed at the microscale in order to derive the governing field equations for the homogenized equivalent medium at the mesoscale, together with the closed form of its constitutive and inertial properties. Therefore, at the mesoscale the material is heterogeneous and composed by two different homogeneous layers. A meso periodic cell $\mathcal{A}_M$ can be thus identified, with $\mathcal{A}_M = [0, L] \times [0, \zeta L_2]$, where $\zeta \to 0$ because of translational invariance existing along direction $\mathbf{e}_1$ of the model at hand. The meso periodic cell $\mathcal{A}_M$, therefore, is characterized by a single periodicity vector $\mathbf{v}_2^M = L\mathbf{e}_2$.

2.2. Constitutive characterization of the metamaterial phases

As introduced in Section 2, the external coating, the connecting elements and the internal ring of the micro periodic cell $\mathcal{A}_m$ are made of steel, which is assumed to exhibit a linear elastic isotropic constitutive response. The polymeric material forming the homogeneous layer at the mesoscale and filling the region between the external coating and the internal ring at the microscale is considered to be characterized by a linear isotropic viscoelastic constitutive behavior. Accordingly, denoting with t the temporal variable, the components of the elastic relaxation tensor $\mathbb{G}(\mathbf{x}, t) = G_{ijhk}(\mathbf{x}, t)\mathbf{e}_i \otimes \mathbf{e}_j \otimes \mathbf{e}_h \otimes \mathbf{e}_k$ are expressed in terms of a Prony series as

$$G_{ijhk}(\mathbf{x}, t) = G_{ijhk}^{(\infty)}(\mathbf{x}) \left[1 + \sum_{n=1}^{N} \mu^n \exp\left(-\frac{t}{\tau_r^n(\mathbf{x})} \right) \right], \tag{1}$$

where $G_{ijhk}^{(\infty)}$ refers to the long term response of the material, μ^n represents the nth viscosity ratio of the relaxation function, and τ_r^n is the nth relaxation time. The bilateral Laplace transform of an arbitrary, time-dependent, real-valued function f is introduced as

$$\mathcal{L}(f(t)) = \hat{f}(s) = \int_{\mathbb{R}} f(t) \exp(-st)\, dt, \tag{2}$$

where Laplace argument $s \in \mathbb{C}$, with $\mathbb{C}$ denoting the set of complex numbers, and the Laplace transform is a complex-valued function, namely $\hat{f} : \mathbb{C} \to \mathbb{C}$. Laplace transform of Eq. (1) leads to

$$\hat{G}_{ijhk} = G_{ijhk}^{(\infty)}(\mathbf{x}) \left(\frac{1}{s} + \sum_{n=1}^{N} \frac{\mu^n \tau_r^n(\mathbf{x})}{s\tau_r^n(\mathbf{x}) + 1} \right). \tag{3}$$

Finally, the piezoelectric phase, which is present within the internal disk of cell $\mathcal{A}_m$, is assumed to exhibit a linear piezoelectric constitutive behavior and to be polarized along the out-of-plane direction. All the piezoelectric phases in the microcells are connected in parallel to an external electrical circuit by means of electrodes. This circuit is characterized by a tunable equivalent admittance/impedance, which affects the constitutive response of the shunting piezoelectric material ultimately enabling to modify the spectral properties of the acoustic metamaterial. Departing from the field equations in the transformed Laplace space for a three-dimensional orthotropic piezoelectric material with out-of-plane polarization, the in-plane components of the transformed stress tensor $\hat{\sigma}_{ij}$ and the transformed electric displacement $\hat{D}_i$, with $i, j = 1, 2$, can be obtained by means of a proper condensation of the corresponding three dimensional constitutive law. This procedure is detailed in [76]. Denoting with subscript $_3$ the tensor components in the out-of-plane direction, and in the assumption of a plane stress state characterized by conditions $\hat{\sigma}_{i3} = 0$, with $i = 1, 2, 3$, and $\hat{I}_3 = 0$, where $\hat{I}_3$ is the transformed current along the out-of-plane direction, the in-plane constitutive equations read

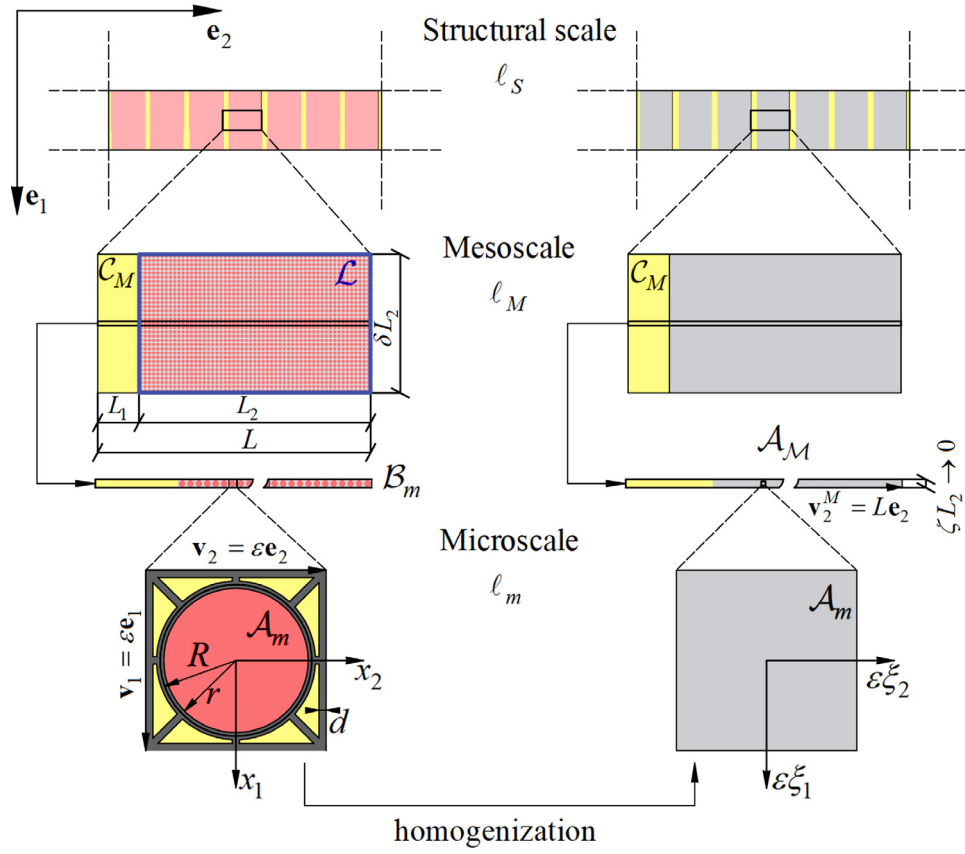$$\hat{\sigma}_{ij} = C_{ijhk}^{EL}(\lambda(s))\hat{u}_{h,k}, \tag{4}$$

Fig. 2. Multiscale representation of the metamaterial: structural, meso and microscales having characteristic lengths ℓ_S, ℓ_M, and ℓ_m, respectively, with $\ell_S \gg \ell_M \gg \ell_m$. The different periodic cells at the appropriate scales and the corresponding periodicity vectors are indicated.

$$\hat{D}_\alpha = -\beta_{\alpha\alpha}^{EL}(\lambda(s)) \frac{\partial \hat{\phi}}{\partial x_\alpha}, \qquad (5)$$

with $i, j, h, k, \alpha = 1, 2$. In Eq. (4), $\hat{u}_h$ and C_{ijhk}^{EL} denote the components of the transformed displacement field and the components of the equivalent fourth-order elasticity tensor, respectively. Further, in Eq. (5), $\hat{\phi}$ is the transformed electric potential and $\beta_{\alpha\alpha}^{EL}$ is the equivalent second-order dielectric permittivity tensor component. Note that from Eq. (5) onward, no summation of index α will be employed. The equivalent fourth-order elasticity tensor and the equivalent second-order dielectric permittivity tensor depend on the tuning parameter λ, which is in turn a function of the complex frequency s as

$$\lambda(s) = \frac{w\, Y_{33}(s)}{s\, \beta_{33} A^{(P)}}, \qquad (6)$$

where w represents the thickness of the piezoelectric disk along the out-of-plane direction and $A^{(P)}$ is the area of the disk. With reference to periodic cell $\mathcal{A}_m$ of Fig. 2, $A^{(P)} = \pi\, r^2$. Moreover, $Y_{33}(s)$ is the s-dependent equivalent shunting admittance that may, in turn, be a function of one or more tuning parameters characterizing the external electrical circuit.

Denoting with e_{ijh} the third-order piezoelectric stress-charge coupling tensor and with $\tilde{e}_{hij} = e_{ijh}$ its transpose, the equivalent elasticity and permittivity tensors read

$$C_{ijhk}^{EL}(\lambda(s)) = C_{ijhk} + \frac{e_{ij3}\tilde{e}_{3hk}}{\beta_{33}^{EL}(\lambda(s))}$$

$$- \left(C_{ij33} + \frac{e_{ij3}\tilde{e}_{333}}{\beta_{33}^{EL}(\lambda(s))} \right) \left(\frac{C_{33hk} + \dfrac{e_{333}\tilde{e}_{3hk}}{\beta_{33}^{EL}(\lambda(s))}}{C_{3333} + \dfrac{e_{333}\tilde{e}_{333}}{\beta_{33}^{EL}(\lambda(s))}} \right), \qquad (7)$$

$$\beta_{\alpha\alpha}^{EL}(\lambda(s)) = \beta_{\alpha\alpha} + \frac{e_{\alpha 3\alpha}\tilde{e}_{\alpha\alpha 3}}{C_{\alpha 3\alpha 3}}, \qquad (8)$$

where $i, j, h, k, \alpha = 1, 2$, and

$$\beta_{33}^{EL}(\lambda(s)) = \beta_{33}\left[1 + \frac{w\, Y_{33}(s)}{s\, \beta_{33}A^{(P)}} \right] = \beta_{33}\left(1 + \lambda(s) \right). \qquad (9)$$

From Eq. (7), it is evident that C_{ijhk}^{EL} preserves minor and major symmetries and that component C_{1212}^{EL} turns out to be s-independent. It is further worth noting that in-plane constitutive Eqs. (4) and (5) written for a piezoelectric medium having an out-of-plane polarization, result to be uncoupled, thus formally resembling the linear elastic dielectric material equations [77].

Because of its technological relevance, from now onward, it is assumed that the equivalent electrical circuit is *purely capacitive* (or non dissipative). In this case, the corresponding purely capacitive equivalent admittance β_{33}^{EL} results to be s-independent and equal to

$$\beta_{33}^{EL} = \beta_{33} + \frac{\mathcal{C}\,w}{A^{(P)}} = \beta_{33}\left(1 + \lambda \right), \qquad (10)$$

with $\mathcal{C}$ the capacitance following from relation $Y_{33}(s) = s\,\mathcal{C}$, with $Y_{33}(s)$ defined by Eq. (9). Tuning parameter λ, therefore, becomes real and linearly dependent upon the capacitance according to

$$\lambda = \frac{\mathcal{C}\,w}{\beta_{33}A^{(P)}}. \qquad (11)$$

In the case of negative capacitance circuits, λ becomes negative as well [78]. Furthermore, if the equivalent circuit is purely capacitive, the components of the equivalent elastic tensor $C_{ijhk}^{EL}(\lambda)$ defined in Eq. (7), reduce to be independent of s. The constitutive properties of the piezoelectric shunting element, therefore, can be controlled by regulating the equivalent impedance of the external

electrical circuit and, in Section 5, it will be demonstrated how this affects the spectral response of the acoustic metadevice at hand. As detailed in [76], for a negative value of λ, which corresponds to a negative purely capacitive equivalent admittance, the stiffness components are characterized by a vertical asymptote in correspondence with the resonance value

$$\lambda_R = -\left(1 + \frac{e_{333}^2}{C_{3333}\beta_{33}}\right). \tag{12}$$

Furthermore, the stiffness components exhibit horizontal asymptotes for $\lambda \to \pm\infty$, which leads to

$$C_{ijhk}^{EL\infty} = \lim_{\lambda \to \pm\infty} C_{ijhk}^{EL}(\lambda) = C_{ijhk} - \frac{C_{ij33}C_{hk33}}{C_{3333}}. \tag{13}$$

Finally, the *open circuit* case occurs when disconnecting the circuit capacitor from the piezoelectric phase or when calibrating a zero capacitance for the equivalent electrical circuit. This corresponds to $\lambda = 0$, for which the stiffness components C_{ijhk}^{EL} read

$$C_{ijhk}^{EL}(\lambda = 0) = C_{ijhk} + \frac{e_{ij3}e_{hk3}}{\beta_{33}}$$
$$- \frac{\left(\beta_{33}C_{ij33} + e_{ij3}e_{333}\right)\left(\beta_{33}C_{hk33} + e_{hk3}e_{333}\right)}{\beta_{33}\left(\beta_{33}C_{3333} + e_{333}^2\right)}. \tag{14}$$

3. Two-scale modeling of the microstructured layer

In this Section, the two-scale asymptotic homogenization technique exploited to derive the overall constitutive and inertial properties of the microstructured layer is summarized. The microscale governing equations are first given in Section 3.1. The asymptotic expansion of the transformed displacement field is detailed in Section 3.2, together with the definition of the cell problems and the down- and up-scaling relations. Finally, the governing field equations for the equivalent homogenized medium and the closed form of its effective constitutive and inertial properties are given in Section 3.3.

3.1. Governing equations

With reference to the micro periodic cell $\mathcal{A}_m$ represented in Fig. 2, the constitutive and inertial properties at the microscale will be denoted by superscript $^{(m,\varepsilon)}$, being ε the size of cell $\mathcal{A}_m$ along $\mathbf{e}_1$ and $\mathbf{e}_2$. In each phase of cell $\mathcal{A}_m$, the transformed microscopic displacement field $\hat{\mathbf{u}} = \hat{u}_i\mathbf{e}_i$ is governed by the equilibrium equation in the transformed Laplace space:

$$\frac{D}{Dx_j}\left(\hat{C}_{ijhk}^{(m,\varepsilon)}(s)\frac{D\hat{u}_h}{Dx_k}\right) + \hat{b}_i = \rho^{(m,\varepsilon)}s^2\hat{u}_i . \tag{15}$$

Here, if the phase is linear viscoelastic, the components of the elastic tensor are written in terms of the components of the micro relaxation tensor as $\hat{C}_{ijhk}^{(m,\varepsilon)}(s) = s\,\hat{G}_{ijhk}^{(m,\varepsilon)}$. Conversely, if the phase is linear elastic, the components of the elastic tensor are s-independent and reduce to $C_{ijhk}^{(m,\varepsilon)}$. In Eq. (15), $\rho^{(m,\varepsilon)}$ represents the mass density of the material and $\hat{b}_i$ are the components of the transformed body forces, which are assumed to have a spatial variability much larger than the microstructural characteristic length scale, consistently with the scale separation condition. In particular, body forces are assumed to be periodic over the cluster of cells $\mathcal{L}$ depicted in Fig. 2, which has characteristic size L_2 (with $L_2 \gg \varepsilon$), and to have a vanishing mean value on $\mathcal{L}$. By virtue of $\mathcal{A}_m$-periodicity of the elasticity tensor and material density, it follows that

$$\hat{C}_{ijhk}^{(m,\varepsilon)}(\mathbf{x} + n\,\mathbf{v}_l, s) = \hat{C}_{ijhk}^{(m,\varepsilon)}(\mathbf{x}, s), \quad \rho^{(m,\varepsilon)}(\mathbf{x} + n\,\mathbf{v}_l) = \rho^{(m,\varepsilon)}(\mathbf{x}),$$
$$\forall \mathbf{x} \in \mathcal{A}_m, \, l = 1, 2, \, n \in \mathbb{Z}. \tag{16}$$

As usually done in asymptotic homogenization, the micro periodic cell $\mathcal{A}_m$ can be rescaled by its size ε, thus obtaining a unit cell $\mathcal{Q} = [0, 1] \times [0, 1]$. Accordingly, periodicity of constitutive and inertial properties can be reformulated as

$$\hat{C}_{ijhk}^{(m,\varepsilon)}(\mathbf{x} + n\,\mathbf{v}_l, s) = \hat{C}_{ijhk}^m\left(\boldsymbol{\xi} = \frac{\mathbf{x}}{\varepsilon}, s\right),$$
$$\rho^{(m,\varepsilon)}(\mathbf{x} + n\,\mathbf{v}_l) = \rho^m\left(\boldsymbol{\xi} = \frac{\mathbf{x}}{\varepsilon}\right), \quad \forall \boldsymbol{\xi} \in \mathcal{Q}, l = 1, 2, \, n \in \mathbb{Z}. \tag{17}$$

This allows to mathematically express the separation of scales by means of two variables: the slow (or mesoscopic) one $\mathbf{x} \in \mathcal{A}_m$ and the fast (or microscopic) one $\boldsymbol{\xi} = \frac{\mathbf{x}}{\varepsilon} \in \mathcal{Q}$. Consequently, the transformed microscale displacement results to be a function of both the slow and the fast space variables and of the complex frequency s, namely $\hat{\mathbf{u}} = \hat{\mathbf{u}}\left(\mathbf{x}, \frac{\mathbf{x}}{\varepsilon}, s\right)$. In the following, the field equations for an equivalent homogeneous medium will be derived in terms of the transformed displacement $\hat{\mathbf{U}}(\mathbf{x}, s) = \hat{U}_i(\mathbf{x}, s)\mathbf{e}_i$ at the mesoscale.

3.2. Asymptotic expansion, cell-problems, down-scaling and up-scaling relations

The transformed microscale displacement field can be asymptotically expanded [58,59] in a series of powers of ε as

$$\hat{u}_k\left(\mathbf{x}, \frac{\mathbf{x}}{\varepsilon}, s\right) = \sum_{l=0}^{\infty} \varepsilon^l \hat{u}_k^{(l)}\left(\mathbf{x}, \frac{\mathbf{x}}{\varepsilon}, s\right) = \hat{u}_k^{(0)}\left(\mathbf{x}, \frac{\mathbf{x}}{\varepsilon}, s\right)$$
$$+ \varepsilon\hat{u}_k^{(1)}\left(\mathbf{x}, \frac{\mathbf{x}}{\varepsilon}, s\right) + \varepsilon^2\hat{u}_k^{(2)}\left(\mathbf{x}, \frac{\mathbf{x}}{\varepsilon}, s\right) + O(\varepsilon^3). \tag{18}$$

Recalling that the generalized derivative of a generic function g with respect to variable x_j takes the form

$$\frac{D}{Dx_j}g\left(\mathbf{x}, \boldsymbol{\xi} = \frac{\mathbf{x}}{\varepsilon}\right) = \left.\left(\frac{\partial g}{\partial x_j} + \frac{1}{\varepsilon}\frac{\partial g}{\partial \xi_j}\right)\right|_{\boldsymbol{\xi}=\frac{\mathbf{x}}{\varepsilon}} = \left.\left(\frac{\partial g}{\partial x_j} + \frac{1}{\varepsilon}g_{,j}\right)\right|_{\boldsymbol{\xi}=\frac{\mathbf{x}}{\varepsilon}}, \tag{19}$$

by substituting expansion (18) into the microscale field Eq. (15) and gathering the terms of equal order of ε, a series of recursive differential problems is obtained:

$$\frac{1}{\varepsilon^2}f_i^{(0)}(\mathbf{x}, s) + \frac{1}{\varepsilon}f_i^{(1)}(\mathbf{x}, s) + \varepsilon^0 f_i^{(2)}(\mathbf{x}, s) + \varepsilon f_i^{(3)}(\mathbf{x}, s)$$
$$+ \ldots + \varepsilon^l f_i^{(l+2)}(\mathbf{x}, s) + \hat{b}_i(\mathbf{x}, s) = 0. \tag{20}$$

In Eq. (20), terms $f_i^{(\alpha)}$, with $\alpha = 0, 1, \ldots, l+2$ represent the volume forces of the relative differential problem at the order $\varepsilon^{\alpha-2}$, which thus depend in space upon the slow variable only.

The solution of problem at the order ε^{-2} is independent of $\boldsymbol{\xi}$ and reads

$$\hat{u}_k^{(0)}(\mathbf{x}, \boldsymbol{\xi}, s) = \hat{U}_k(\mathbf{x}, s), \tag{21}$$

because of its solvability condition in the class of $\mathcal{Q}$−periodic functions. For details on the derivation of the solutions of the recursive differential problems (20), the reader may refer to [64, 65]. Taking into account solution (21) at order ε^{-2} and the $\mathcal{Q}$-periodicity of tensor $\hat{\mathbf{c}}^m = \hat{C}_{ijhk}^m \mathbf{e}_i \otimes \mathbf{e}_j \otimes \mathbf{e}_h \otimes \mathbf{e}_k$, solvability condition for the problem at order ε^{-1} implies that the solution has the form

$$\hat{u}_k^{(1)}(\mathbf{x}, \boldsymbol{\xi}, s) = N_{kpq_1}^{(1)}(\boldsymbol{\xi}, s)\frac{\partial \hat{U}_p(\mathbf{x}, s)}{\partial x_{q_1}}, \tag{22}$$

where $N_{kpq_1}^{(1)}$ is the corresponding perturbation function. Analogously, considering solution (21) of problem at order ε^{-2} and

solution (22) of problem at order ε^{-1}, the solution at order ε^0 reads

$$\hat{u}_k^{(2)}(\mathbf{x},\boldsymbol{\xi},s) = N_{kpq_1q_2}^{(2)}(\boldsymbol{\xi},s)\frac{\partial^2 \hat{U}_p(\mathbf{x},s)}{\partial x_{q_1} \partial x_{q_2}} + N_{kp}^{(2,2)}(\boldsymbol{\xi},s)s^2 \hat{U}_p(\mathbf{x},s), \quad (23)$$

where $N_{kpq_1q_2}^{(2)}$ and $N_{kp}^{(2,2)}$ are the corresponding perturbation functions.

In general, perturbation functions are smooth $\mathcal{Q}$-periodic functions that illustrate the role of the microstructural heterogeneities on $\hat{\mathbf{u}}$ and, as such, depend upon $\boldsymbol{\xi}$ (as well as upon the complex frequency s). In order to guarantee the uniqueness of solution of the relative differential problem, the perturbation functions are required to vanish on average on the unit cell, according to the normalization condition

$$\langle (\cdot) \rangle = \frac{1}{|\mathcal{Q}|} \int_{\mathcal{Q}} (\cdot)\, d\boldsymbol{\xi} = 0\,, \quad (24)$$

where $|\mathcal{Q}|$ is the area of the unit cell.

Perturbation functions are obtained by solving the corresponding non-homogeneous differential problems called *cell problems*. In particular, functions $N_{kpq_1}^{(1)}$ are the solution of the order ε^{-1} cell problem, i.e.

$$\left(\hat{C}_{ijhk}^m N_{hpq_1,k}^{(1)}\right)_{,j} + \hat{C}_{ijpq_1,j}^m = 0\,. \quad (25)$$

Two different cell problems arise at order ε^0. The first one is in terms of $N_{kpq_1q_2}^{(2)}$ and has the following expression, symmetrized with respect to indices q_1 and q_2:

$$\left(\hat{C}_{ijhk}^m N_{hpq_1q_2,k}^{(2)}\right)_{,j} + \frac{1}{2}\left[\left(\hat{C}_{ijhq_2}^m N_{hpq_1}^{(1)} + \hat{C}_{ijhq_1}^m N_{hpq_2}^{(1)}\right)_{,j}\right.$$
$$\left. + \hat{C}_{iq_1pq_2}^m + \hat{C}_{iq_2pq_1}^m + \hat{C}_{iq_2hj}^m N_{hpq_1,j}^{(1)} + \hat{C}_{iq_1hj}^m N_{hpq_2,j}^{(1)}\right]$$
$$= \frac{1}{2}\left\langle \hat{C}_{iq_1pq_2}^m + \hat{C}_{iq_2hj}^m N_{hpq_1,j}^{(1)} + \hat{C}_{iq_2pq_1}^m \hat{C}_{iq_1hj}^m N_{hpq_2,j}^{(1)}\right\rangle. \quad (26)$$

The second cell problem provides perturbation function $N_{hp}^{(2,2)}$ and reads

$$\left(\hat{C}_{ijhk}^m N_{hp,k}^{(2,2)}\right)_{,j} - \rho^m \delta_{ip} = -\left\langle \rho^m \right\rangle \delta_{ip}\,. \quad (27)$$

Higher-order cell problems are not specified for the sake of briefness, but they can be determined by carrying out a similar procedure to that detailed above. Once the solution of the cell problems is known, the expansion (18) can be rewritten in the form of the so-called down-scaling relation, namely

$$\hat{u}_h\left(\mathbf{x},\frac{\mathbf{x}}{\varepsilon},s\right) = \left[\hat{U}_h(\mathbf{x},s) + \varepsilon N_{hpq_1}^{(1)}(\boldsymbol{\xi},s)\frac{\partial \hat{U}_p(\mathbf{x},s)}{\partial x_{q_1}}\right.$$
$$+ \varepsilon^2 \left(N_{hpq_1q_2}^{(2)}(\boldsymbol{\xi},s)\frac{\partial^2 \hat{U}_p(\mathbf{x},s)}{\partial x_{q_1}\partial x_{q_2}}+\right.$$
$$\left.\left.+ N_{hp}^{(2,2)}(\boldsymbol{\xi},s)s^2\hat{U}_p(\mathbf{x},s)\right) + O(\varepsilon^3)\right]\Bigg|_{\boldsymbol{\xi}=\frac{\mathbf{x}}{\varepsilon}}, \quad (28)$$

where the microscale transformed displacement $\hat{\mathbf{u}}$ is related to the corresponding mesoscopic variable $\hat{\mathbf{U}}$ and its gradients.

The up-scaling relation defines transformed mesoscopic displacement as the mean value of the microscale displacement over $\mathcal{Q}$, namely

$$\hat{U}_h(\mathbf{x},s) \doteq \left\langle \hat{u}_h\left(\mathbf{x},\frac{\mathbf{x}}{\varepsilon}+\boldsymbol{\zeta},s\right)\right\rangle_{\boldsymbol{\zeta}}\,. \quad (29)$$

Translation variable $\boldsymbol{\zeta}$ in Eq. (29) is defined such that $\varepsilon\boldsymbol{\zeta} \in \mathcal{A}_m$ and has the role of removing rapid fluctuations of coefficients [79,80].

Invariance property

$$\langle g(\boldsymbol{\xi}+\boldsymbol{\zeta})\rangle_{\boldsymbol{\zeta}} = \frac{1}{|\mathcal{Q}|}\int_{\mathcal{Q}} g(\boldsymbol{\xi}+\boldsymbol{\zeta})\, d\boldsymbol{\zeta} = \frac{1}{|\mathcal{Q}|}\int_{\mathcal{Q}} g(\boldsymbol{\xi}+\boldsymbol{\zeta})\, d\boldsymbol{\xi}, \quad (30)$$

proved to hold for each $\mathcal{Q}$-periodic function, together with condition (24), leads to up-scaling relation (29).

3.3. Overall constitutive and inertial properties

In the following, a variational-asymptotic procedure is employed to derive the field equations for the equivalent homogeneous continuum in terms of the overall constitutive and inertial properties. Generally speaking, by imposing the stationarity of the first-order variation of a suitable functional (truncated at a proper order) it is possible to obtain, in an energetically-consistent manner, local and non-local constitutive and inertial terms that automatically satisfy symmetry and positive definiteness requirements [79,81]. In this context, the field equation for a first-order equivalent medium is provided. To this purpose, functional $\hat{\Phi}$ is defined in terms of the transformed microscopic energy density $\hat{\phi}\left(\mathbf{x},\frac{\mathbf{x}}{\varepsilon},s\right)$ as

$$\hat{\Phi} = \int_{\mathcal{L}} \hat{\phi}\left(\mathbf{x},\frac{\mathbf{x}}{\varepsilon},s\right) d\mathbf{x}$$
$$= \int_{\mathcal{L}} \left(\frac{1}{2}s^2\rho^m\hat{\mathbf{u}}\cdot\hat{\mathbf{u}} + \frac{1}{2}\nabla\hat{\mathbf{u}}:\hat{\mathfrak{c}}^m:\nabla\hat{\mathbf{u}} - \hat{\mathbf{b}}\cdot\hat{\mathbf{u}}\right)d\mathbf{x}\,. \quad (31)$$

The corresponding Euler–Lagrange equation is the micro field Eq. (15). Symbol : in Eq. (31) represents the tensorial double contraction inner product. The transformed energy density satisfies the condition $\hat{\phi}\left(\mathbf{x},\frac{\mathbf{x}}{\varepsilon},s\right) = \hat{\phi}\left(\mathbf{x},\frac{\mathbf{x}}{\varepsilon}+\boldsymbol{\zeta},s\right)$, for which functional $\hat{\Phi}$ can be consequently expressed in terms of the translation variable $\boldsymbol{\zeta}$ as

$$\hat{\Phi}^{\zeta} = \hat{\Phi}(\boldsymbol{\zeta}) = \int_{\mathcal{L}} \hat{\phi}^{\zeta}\left(\mathbf{x},\frac{\mathbf{x}}{\varepsilon},s\right)d\mathbf{x} = \int_{\mathcal{L}} \hat{\phi}\left(\mathbf{x},\frac{\mathbf{x}}{\varepsilon}+\boldsymbol{\zeta},s\right)d\mathbf{x}\,. \quad (32)$$

Taking into account that

$$\left\langle \hat{\phi}\left(\mathbf{x},\frac{\mathbf{x}}{\varepsilon}+\boldsymbol{\zeta},s\right)\right\rangle = \frac{1}{|\mathcal{Q}|}\int_{\mathcal{Q}} \hat{\phi}\left(\mathbf{x},\frac{\mathbf{x}}{\varepsilon}+\boldsymbol{\zeta},s\right)d\boldsymbol{\zeta}$$
$$= \frac{1}{|\mathcal{Q}|}\int_{\mathcal{Q}} \hat{\phi}(\mathbf{x},\boldsymbol{\xi},s)\,d\boldsymbol{\xi} = \left\langle \hat{\phi}(\mathbf{x},\boldsymbol{\xi},s)\right\rangle, \quad (33)$$

the average functional $\hat{\Phi}_m$ at the microscale is defined as

$$\hat{\Phi}_m \doteq \left\langle \hat{\Phi}^{\zeta}\right\rangle = \frac{1}{|\mathcal{Q}|}\int_{\mathcal{Q}} \hat{\Phi}^{\zeta}d\boldsymbol{\zeta} = \int_{\mathcal{L}}\left\langle \hat{\phi}\left(\mathbf{x},\frac{\mathbf{x}}{\varepsilon}+\boldsymbol{\zeta},s\right)\right\rangle d\mathbf{x}, \quad (34)$$

where the order of integration has been changed in virtue of Fubini's theorem. By using down-scaling relation (28), functional (31) can be expressed in terms of the transformed mesoscopic displacement $\hat{\mathbf{U}}$ as

$$\hat{\Phi}_m = \frac{1}{2}s^2\left\langle \rho^m\right\rangle\int_{\mathcal{L}}\hat{U}_h\hat{U}_h d\mathbf{x} + \left\langle \frac{1}{2}B_{ijlr_1}^{(1)}\hat{C}_{ijhk}^m B_{hkpq_1}^{(1)}\right\rangle\int_{\mathcal{L}}\frac{\partial \hat{U}_l}{\partial x_{r_1}}\frac{\partial \hat{U}_p}{\partial x_{q_1}}d\mathbf{x}$$
$$- \int_{\mathcal{L}}\hat{U}_h\hat{b}_h\, d\mathbf{x} + O(\varepsilon^2), \quad (35)$$

where, recalling derivation rule (19), generalized derivative of $\hat{\mathbf{u}}$ can be expressed as

$$\frac{D\hat{u}_h}{Dx_k} = B_{hkpq_1}^{(1)}\frac{\partial \hat{U}_p}{\partial x_{q_1}} + O(\varepsilon). \quad (36)$$

Formula (36) introduces the localization tensor $B_{hkpq_1}^{(1)}$, which is a function of the perturbation function $N_{hpq_1}^{(1)}$ and, consequently, is $\mathcal{Q}$-periodic. More specifically, $B_{hkpq_1}^{(1)}$ is defined as $B_{hkpq_1}^{(1)} =$

$\delta_{hp}\delta_{kq_1} + N^{(1)}_{hpq_1,k}$. By exploiting the divergence theorem and the $\mathcal{Q}$-periodicity of the localization tensor $B^{(1)}_{hkpq_1}$ and of the micro constitutive tensor $\hat{C}^m_{ijhk}$, it is possible to prove that the Euler–Lagrange equation of functional $\hat{\Phi}_m$, truncated at the zero-*th* order in ε, is

$$\hat{C}_{lr_1pq_1}\frac{\partial^2 \hat{U}_p}{\partial x_{q_1}\partial x_{r_1}} + \hat{b}_l = \rho s^2 \hat{U}_l, \tag{37}$$

which is exactly the field equation of the first-order homogenized medium. The transformed overall constitutive tensor $\hat{C}_{lr_1pq_1}$ and the overall density ρ, therefore, have the form

$$\hat{C}_{lr_1pq_1} = \left\langle B^{(1)}_{ijlr_1}\hat{C}^m_{ijhk}B^{(1)}_{hkpq_1}\right\rangle, \tag{38}$$

$$\rho = \left\langle \rho^m \right\rangle. \tag{39}$$

4. Frequency band structure for the multilayered medium

The two-scale homogenization technique described in Section 3 allows to treat the multilayered material at the mesoscale as if each layer is homogeneous. Recalling Fig. 2, at the mesoscale, the periodic cell $\mathcal{A}_M$ can be identified, which is composed of $n = 2$ different layers and is characterized by a periodicity vector $\mathbf{v}^M_2 = L\mathbf{e}_2$ perpendicular to material layering and by a vanishing characteristic size along the layering because of translational invariance along $\mathbf{e}_1$ direction. Since free Bloch wave propagation inside the metamaterial will be investigated, in case of vanishing body forces $\hat{\mathbf{b}}$, from Eq. (37), the transformed mesoscale field equation governing the behavior of the resulting heterogeneous multilayered medium reads

$$\frac{\partial}{\partial x_j}\left(\hat{C}_{ijhk}(x_2, s)\frac{\partial \hat{U}_h(x_1, x_2, s)}{\partial x_k}\right) - s^2\rho(x_2)\hat{U}_i(x_1, x_2, s) = 0. \tag{40}$$

In Eq. (40), $\hat{C}_{ijhk}$ are the components of the relaxation tensor and ρ is the mass density. These properties are defined at the mesoscale; accordingly, their values depend upon the specific layer they refer to. Therefore, relaxation tensor $\hat{\mathfrak{c}}(x_2, s) = \hat{C}_{ijhk}(x_2, s)\mathbf{e}_i\otimes\mathbf{e}_j\otimes\mathbf{e}_h\otimes\mathbf{e}_k$ and density $\rho(x_2)$ are $\mathcal{A}_M$-periodic and do not depend upon coordinate x_1 because of translational invariance characterizing the meso cell $\mathcal{A}_M$ along $\mathbf{e}_1$ direction. By virtue of the $\mathcal{A}_M$-periodicity of the medium, solution $\hat{\mathbf{U}}$ of Eq. (40) can be written by employing the Floquet–Bloch decomposition as

$$\hat{\mathbf{U}}(x_1, x_2, s) = \hat{\mathbf{U}}^B(x_2, s)\exp[i(\mathbf{k}\cdot\mathbf{x})], \tag{41}$$

where $\mathbf{k} = k_i\mathbf{e}_i$ is the wave vector and vector $\hat{\mathbf{U}}^B(x_2, s) = \hat{U}^B_i(x_2, s)\mathbf{e}_i$ contains the $\mathcal{A}_M$-periodic Bloch amplitudes, and i is the imaginary unit. Once again, the latter does not depend upon x_1 because of the translational invariance of periodic cell $\mathcal{A}_M$ along the direction parallel to material layering. It spatially depends only upon the coordinate perpendicular to the material layering (in this case x_2) when the phases of the multilayered material are orthotropic with the orthotropy axis parallel or perpendicular to the layering.

By inserting decomposition (41) into Eq. (40), and by applying simple algebraic derivations, it is possible to obtain a system of second-order ordinary differential equations that express field equations for each single layer in terms of Bloch amplitude as

$$\hat{C}_{1212}\hat{U}^B_{1,22} + 2ik_2\hat{C}_{1212}\hat{U}^B_{1,2} + ik_1\left(\hat{C}_{1212} + \hat{C}_{1122}\right)\hat{U}^B_{2,2}$$

$$+\left(-\rho s^2 - k_1^2\hat{C}_{1111} - k_2^2\hat{C}_{1212}\right)\hat{U}^B_1 +$$

$$-k_1k_2\left(\hat{C}_{1212} + \hat{C}_{1122}\right)\hat{U}^B_2 = 0, \tag{42}$$

$$\hat{C}_{2222}\hat{U}^B_{2,22} + 2ik_2\hat{C}_{2222}\hat{U}^B_{2,2} + ik_1\left(\hat{C}_{1212} + \hat{C}_{1122}\right)\hat{U}^B_{1,2}$$

$$+\left(-\rho s^2 - k_1^2\hat{C}_{1212} - k_2^2\hat{C}_{2222}\right)\hat{U}^B_2 +$$

$$-k_1k_2\left(\hat{C}_{1212} + \hat{C}_{1122}\right)\hat{U}^B_1 = 0, \tag{43}$$

where derivatives with respect to x_2 are now classical derivatives. System of Eqs. (42)–(43) can be expressed in operatorial form as

$$\mathbf{A}\,\hat{\mathbf{U}}^B_{,22} + \mathbf{B}\,\hat{\mathbf{U}}^B_{,2} + \mathbf{C}\,\hat{\mathbf{U}}^B = \mathbf{0}, \tag{44}$$

where matrices $\mathbf{A}$, $\mathbf{B}$, and $\mathbf{C}$ read

$$\mathbf{A} = \begin{pmatrix} \hat{C}_{1212} & 0 \\ 0 & \hat{C}_{2222} \end{pmatrix},$$

$$\mathbf{B} = \begin{pmatrix} 2ik_2\hat{C}_{1212} & ik_1(\hat{C}_{1212} + \hat{C}_{1122}) \\ ik_1(\hat{C}_{1122} + \hat{C}_{1212}) & 2ik_2\hat{C}_{2222} \end{pmatrix},$$

$$\mathbf{C} = \begin{pmatrix} -\rho s^2 - k_1^2\hat{C}_{1111} - k_2^2\hat{C}_{1212} & -k_1k_2\left(\hat{C}_{1122} + \hat{C}_{1212}\right) \\ -k_1k_2\left(\hat{C}_{1122} + \hat{C}_{1212}\right) & -\rho s^2 - k_1^2\hat{C}_{1212} - k_2^2\hat{C}_{2222} \end{pmatrix}. \tag{45}$$

Defining vector $\mathbf{r} = \left(\hat{\mathbf{U}}^B_{,2}\ \hat{\mathbf{U}}^B\right)^T$, it is possible to reduce the order of system (44) doubling its dimension as

$$\mathbf{M}\mathbf{r}_{,2} + \mathbf{N}\mathbf{r} = \mathbf{0}, \tag{46}$$

with $\mathbf{M}$ a 4×4 non singular square diagonal block matrix and $\mathbf{N}$ a square block matrix defined as

$$\mathbf{M} = \begin{pmatrix} \mathbf{A} & \mathbf{0} \\ \mathbf{0} & \mathbf{I} \end{pmatrix}, \quad \mathbf{N} = \begin{pmatrix} \mathbf{B} & \mathbf{C} \\ -\mathbf{I} & \mathbf{0} \end{pmatrix}, \tag{47}$$

where $\mathbf{I}$ is the identity matrix. First-order ordinary differential system of Eqs. (46) admits the general solution

$$\mathbf{r} = \exp\left[\mathbf{M}^{-1}\mathbf{N}x_2\right]\mathbf{c}, \tag{48}$$

in which $\mathbf{c}$ is a vector of constants and $\exp[\cdot]$ indicates the exponential matrix, which can be computed by following different techniques [82]. Vector $\hat{\mathbf{S}}(x_1, x_2, s)$ contains the transformed stress components $\hat{S}_{12}(x_1, x_2, s)$ and $\hat{S}_{22}(x_1, x_2, s)$ expressed resorting Floquet–Bloch decomposition and is expressed as

$$\hat{\mathbf{S}}(x_1, x_2, s) = \left(\hat{S}^B_{12}(x_2, s)\ \hat{S}^B_{22}(x_2, s)\right)^T \exp\left[i\left(\mathbf{k}\cdot\mathbf{x}\right)\right], \tag{49}$$

with $\hat{S}^B_{12}$ and $\hat{S}^B_{22}$ the corresponding $\mathcal{A}_M$-periodic Bloch amplitudes. Gathering expressions (41) and (49) into vector $\hat{\mathbf{Y}}$ results in

$$\hat{\mathbf{Y}}(x_1, x_2, s) = \begin{pmatrix} \hat{\mathbf{U}}(x_1, x_2, s) \\ \hat{\mathbf{S}}(x_1, x_2, s) \end{pmatrix} = \exp\left[i(\mathbf{k}\cdot\mathbf{x})\right]\begin{pmatrix} \mathbf{0} & \mathbf{I} \\ \mathbf{A} & i\mathbf{A}k_2 \end{pmatrix}\mathbf{r}, \tag{50}$$

where $\mathbf{A}$ is the diagonal matrix defined in Eq. (45). If the thickness of the generic qth layer of the multilayered material along direction $\mathbf{e}_2$ is denoted as L_q, and $\hat{\mathbf{Y}}^+_q$ and $\hat{\mathbf{Y}}^-_q$ refer to vector $\hat{\mathbf{Y}}$ computed at the upper and lower boundaries of the layer, respectively, simple algebraic manipulations lead to

$$\hat{\mathbf{Y}}^+_q = \begin{pmatrix} \mathbf{0} & \mathbf{I} \\ \mathbf{A} & i\mathbf{A}k_2 \end{pmatrix}\exp\left[-\mathbf{M}^{-1}\mathbf{N}L_q\right]\begin{pmatrix} \mathbf{0} & \mathbf{I} \\ \mathbf{A} & i\mathbf{A}k_2 \end{pmatrix}^{-1}$$

$$\times \exp\left[i\,k_2\,L_q\right]\hat{\mathbf{Y}}^-_q = \mathbf{T}_q\,\hat{\mathbf{Y}}^-_q. \tag{51}$$

Formula (51) introduces the frequency-dependent transfer matrix of the qth layer $\mathbf{T}_q$, which is a symplectic matrix with a unitary determinant [83]. The condition of perfect bond assumed at the interface between two adjacent layers, namely $\hat{\mathbf{Y}}^+_q = \hat{\mathbf{Y}}^-_{q+1}$, enables to express vector $\hat{\mathbf{Y}}^+_n$ at the upper boundary of the last nth layer in terms of the same quantity at the lower boundary of the

first layer $\hat{\mathbf{Y}}_1^-$ through the frequency- and k_1-dependent transfer matrix of the entire periodic cell $\mathcal{A}_M$ as

$$\hat{\mathbf{Y}}_n^+ = \mathbf{T}_{(1,n)}\hat{\mathbf{Y}}_1^-, \tag{52}$$

with $\mathbf{T}_{(1,n)} = \prod_{i=0}^{n-1} \mathbf{T}_{n-i}$. Furthermore, periodicity of cell $\mathcal{A}_M$ along the x_2 direction links the two previous vectors through the Floquet–Bloch boundary condition as

$$\hat{\mathbf{Y}}_n^+ = \exp[i\,k_2\,L]\,\hat{\mathbf{Y}}_1^-, \tag{53}$$

where $L = \sum_{q=1}^n L_q$ is the total length of cell $\mathcal{A}_M$ along x_2. The two conditions (52) and (53) result in the non-linear eigenproblem

$$\left(\mathbf{T}_{(1,n)} - \gamma\mathbf{I}\right)\hat{\mathbf{Y}}_1^- = \mathbf{0}. \tag{54}$$

Eq. (54) allows to investigate in-plane propagation of waves by imposing the singularity of the coefficients matrix, which leads to the characteristic equation

$$\mathcal{D}(\mathbf{k}, s) = \text{Det}\left(\mathbf{T}_{(1,n)} - \gamma\mathbf{I}\right) = 0. \tag{55}$$

This relation characterizes in an implicit form the frequency band structure of the composite material. Because of its technological relevance, from now on, it will be assumed that waves propagate only in the direction perpendicular to material layering (namely $k_1 = 0$). As a consequence, Eq. (54) becomes a standard eigenproblem with eigenvalue γ, which also plays the role of Floquet multiplier, and eigenvector $\hat{\mathbf{Y}}_1^-$, which is the polarization vector of the propagating wave. In this case, the characteristic polynomial associated to dispersion relation (55), due to the simplecticity property of transfer matrix $\mathbf{T}_{(1,n)}$ [84,85], specializes into the form

$$\mathcal{P}(\gamma) = \gamma^4 + I_1\,\gamma^3 + I_2\,\gamma^2 + I_1\,\gamma + 1, \tag{56}$$

in terms of invariants I_1 and I_2. Furthermore, if γ_k is the kth eigenvalue of problem (54), also $1/\gamma_k$ is an eigenvalue for it, because of palindromy property of the characteristic polynomial. Polynomial (56) can be decomposed as the product of two 2nd-order polynomials as

$$\mathcal{P}(\gamma) = \left(\gamma^2 + I_1^L\,\gamma + 1\right)\left(\gamma^2 + I_1^S\,\gamma + 1\right), \tag{57}$$

with I_1^L and I_1^S representing the first invariants related to longitudinal and shear waves, respectively. They read $I_1^\alpha = -\text{Trace}\left(\mathbf{T}_{(1,n)}^\alpha\right)$, with $\alpha = L$ or S and $\mathbf{T}_{(1,n)}^\alpha$ the transfer matrix for the corresponding waves propagation problem. Invariant I_1^α, can be expressed in terms of the constitutive and geometrical properties of the multilayered structure at the mesoscale, as depicted in Fig. 2, and in terms of frequency ω as

$$I_1^\alpha = \frac{1}{\hat{C}_{\beta2\beta2}^{[1]}\,\rho^{[1]}\hat{C}_{\beta2\beta2}^{[2]}\,\rho^{[2]}}$$

$$\times \left[\sin\left(\frac{L_1\,\omega\sqrt{\hat{C}_{\beta2\beta2}^{[1]}\,\rho^{[1]}}}{\hat{C}_{\beta2\beta2}^{[1]}}\right)\sqrt{\hat{C}_{\beta2\beta2}^{[1]}\,\rho^{[1]}\,\hat{C}_{\beta2\beta2}^{[2]}\,\rho^{[2]}}\,\times\right.$$

$$\times\left(\hat{C}_{\beta2\beta2}^{[1]}\,\rho^{[1]} + \hat{C}_{\beta2\beta2}^{[2]}\,\rho^{[2]}\right)\sin\left(\frac{L_2\,\omega\sqrt{\hat{C}_{\beta2\beta2}^{[2]}\,\rho^{[2]}}}{\hat{C}_{\beta2\beta2}^{[2]}}\right)$$

$$-2\,\hat{C}_{\beta2\beta2}^{[1]}\,\rho^{[1]}\,\hat{C}_{\beta2\beta2}^{[2]}\,\rho^{[2]}\times$$

$$\left.\times\cos\left(\frac{L_1\,\omega\sqrt{\hat{C}_{\beta2\beta2}^{[1]}\,\rho^{[1]}}}{\hat{C}_{\beta2\beta2}^{[1]}}\right)\cos\left(\frac{L_2\,\omega\sqrt{\hat{C}_{\beta2\beta2}^{[2]}\,\rho^{[2]}}}{\hat{C}_{\beta2\beta2}^{[2]}}\right)\right], \tag{58}$$

where superscripts [1] and [2] indicate quantities related to the homogeneous polymeric layer and to the homogenized microstructured layer, respectively. For the stiffness components $\hat{C}_{\beta2\beta2}$, $\beta = 1$ for shear waves ($\alpha = S$) and $\beta = 2$ for longitudinal waves

($\alpha = L$). Further, L_1 and L_2 are the lengths of the polymeric and of the microstructured layer, respectively, along direction $\mathbf{e}_2$. If $I_1^\alpha \in [-2, 2]$, the corresponding angular frequency ranges identify pass bands for the related wave problem, while ω intervals for which I_1^α values fall outside of $[-2, 2]$ denote the presence of band gaps.

Once the invariants I_1^α have been computed through relation (58), considering Eq. (57), complex eigenvalue γ^α can be simply obtained as the root of a second-order equation, whereby the magnitude can be expressed as

$$\left|\gamma_\pm^\alpha\right| = \frac{1}{16}\left(\pm\sqrt{\left|I_1^{\alpha2} - 4\right|}\,\text{sgn}\left(I_1^{\alpha2} - 4\right) + 2\,I_1^\alpha \pm \sqrt{\left|I_1^{\alpha2} - 4\right|}\right)^2 +$$

$$+\frac{1}{16}\left|I_1^{\alpha2} - 4\right|\left(-1 + \text{sgn}\left(I_1^{\alpha2} - 4\right)\right)^2, \tag{59}$$

where $\text{sgn}(\cdot)$ represents the signum function. By imposing that $\left|\gamma_\pm^\alpha\right| = 1$, the limit values of I_1^α in correspondence of which there is a pass band, are obtained. In particular, pass bands are detected for $-2 \leq I_1^\alpha \leq 2$. Values of I_1^α outside of the interval $[-2, 2]$ denote stop bands for progressive or reversive waves. In order to obtain the complete frequency spectrum for the metamaterial, Eq. (55) has to be solved in terms of wave vector $\mathbf{k}$ and angular frequency s, which can be both complex − see for details [86,87]. With the aim of investigating spatial damping for the metadevice at hand, Eq. (55) specializes to the case of a complex wave vector (i.e. $k_\alpha = k_{\alpha r} + i\,k_{\alpha i}$ with $\alpha = 1, 2$) and frequency $s = i\omega$ with $\omega \in \mathbb{R}$. It is worth noting that in this case, where k_1 is fixed, matrix $\mathbf{T}_{(1,n)}$ results to be independent of component k_2. Therefore, since $k_2 = \ln(\gamma)/(iL)$, real and imaginary components of k_2 can be obtained from the real and imaginary parts of the Floquet multiplier γ, with $\gamma = \gamma_r + i\gamma_i$, as

$$k_{2r} = \text{Arg}\frac{\gamma_r + i\,\gamma_i}{L}, \qquad k_{2i} = -\frac{1}{2}\frac{\ln\left(\gamma_r^2 + \gamma_i^2\right)}{L}, \tag{60}$$

where $\text{Arg}(\cdot)$ denotes the argument of a complex number.

5. Results

This Section illustrates the filtering properties of the proposed metadevice. The geometrical and material parameters used in the analyses are first introduced in Section 5.1. The overall tunable frequency-dependent constitutive properties for the homogenized material at the mesoscale and the corresponding microscopic local fields, which have been determined according to the asymptotic homogenization procedure, are discussed in Section 5.2. Finally, Section 5.3 presents the obtained frequency band structure for the metadevice, with emphasis on the effects of the tuning parameter on the filtering features.

5.1. Geometrical and material input parameters for the analyses

Consider the micro periodic cell $\mathcal{A}_m$, illustrated in Fig. 2, which has been assumed to be a square domain with edge size equal to ε. The external coating, the internal ring, and the eight connecting elements have all thickness d, which is defined with respect to the cell size such that $d/\varepsilon = 0.0250$. The mean radius R of the internal ring is also prescribed in terms of ε, with $R/\varepsilon = 0.4400$, from which the inner radius r follows as $r = R - d/2$, i.e. $r/\varepsilon = 0.4275$. Finally, the ratio between the out-of-plane thickness w and the size ε is prescribed as $w/\varepsilon = 1$.

The external coating, the internal ring, and the connecting elements (gray color in Fig. 2) are made of steel, which is assumed as a linear elastic isotropic material with Young's modulus $E = 210$ GPa, Poisson's ratio $\nu = 0.3$, and mass density $\rho = 7500$ kg/m^3. The polymeric phase, indicated by the yellow color in Fig. 2, is considered to be made of Epotex 301, which shows a linear viscoelastic isotropic constitutive behavior, with Young's

modulus $E = 3.6$ GPa, Poisson's ratio $\nu = 0.35$, and mass density $\rho = 1150$ kg/m^3. Truncating Prony series (1) at $N = 1$, the viscosity ratio of the relaxation function μ is here assumed to have a unit value, while the relaxation time τ_r is equal to 10^{-3} s. Note that this polymeric material is present both in the micro periodic cell $\mathcal{A}_m$ and in the homogeneous layer at the mesoscale. Lastly, the shunting piezoelectric phase constituting the internal disk of the micro periodic cell $\mathcal{A}_m$ (red color in Fig. 2) is made by Polyvinylidene fluoride (PVDF), which exhibits a linear piezoelectric constitutive behavior. The electromechanical properties of PVDF, which is considered to be polarized along the out-of-plane direction, are represented by the non-vanishing components of the fourth order elasticity tensor $C_{1111} = C_{2222} = 4.84$ GPa, $C_{3333} = 4.63$ GPa, $C_{1122} = 2.72$ GPa, $C_{1133} = C_{2233} = 2.22$ GPa, $C_{1212} = 1.06$ GPa and $C_{1313} = C_{2323} = 5.26 \cdot 10^7$ Pa, of the third order stress-charge coupling tensor $e_{113} = e_{223} = -1.999 \cdot 10^{-3}$ C/m^2, $e_{311} = e_{322} = 4.344 \cdot 10^{-3}$ C/m^2, and $e_{333} = -1.099 \cdot 10^{-3}$ C/m^2, and of the second-order dielectric permittivity tensor $\beta_{11} = \beta_{22} = 6.641 \cdot 10^{-11}$ C/V m and $\beta_{33} = 7.083 \cdot 10^{-11}$ C/V m. Finally, the mass density of PVDF is taken as $\rho = 1780$ kg/m^3.

5.2. Local and effective tunable frequency-dependent response of the multiphase microscopic cell

The local and effective response of the microscale piezoelectric shunting cell $\mathcal{A}_m$ are computed for a set of values of the tuning parameter λ, which vary in the range $\lambda \in [-3, \lambda_R) \cup (\lambda_R, 1]$. The resonance value λ_R is obtained according to Eq. (12) and, for the material properties given in Section 5.1, specifies as $\lambda_R \approx -1.03682961$. Further, the results are presented in terms of the dimensionless angular frequency $\omega^* = \omega/\omega_{ref}$, with the reference frequency $\omega_{ref} = 1$ rad/s and $\omega^* \in \frac{1}{\tau_r \omega_{ref}}[0, 2 \cdot 10^4] = [0, 2 \cdot 10^7]$.

As introduced in Section 3.2, perturbation functions $N_{kpq_1}^{(1)}$ are solutions of cell problem (25) and describe the microfluctuation of the displacement field component $\hat{u}_k$, due to the gradient of the mesoscopic displacement $\partial \hat{U}_p(\mathbf{x}, s)/\partial x_{q_1}$. Fig. 3 illustrates the perturbation function component $N_{111}^{(1)}$ over the microscale unit cell Q in the case of $\omega^* = 0$, which refers to the quasi-static response of the viscoelastic phase, for two different values of the tuning parameter λ, corresponding to the case of an open circuit ($\lambda = 0$) and to the resonance value ($\lambda \to \lambda_R^+$). Note that for $\omega^* = 0$, the perturbation function is characterized by the real part only, with $N_{kpq_1}^{(1)} = \text{Re}(N_{kpq_1}^{(1)})$. Moreover, it can be observed from Fig. 3 that the choice of the tuning parameter λ strongly affects the local displacement field in the microscale cell, whereby the magnitude of the perturbation function substantially increases when approaching the resonance value λ_R.

In the general case of $\omega^* > 0$, the perturbation function $N_{kpq_1}^{(1)}$ is a complex number. The imaginary part $\text{Im}(N_{111}^{(1)})$ and the magnitude $|N_{111}^{(1)}|$ of the perturbation function component $N_{111}^{(1)}$ are presented in Fig. 4 for $\omega^* = 10^4$, and considering $\lambda = 0$ and $\lambda \to \lambda_R^+$. The real part of the perturbation function is qualitatively comparable to that shown in Fig. 3 and is thus omitted for brevity. Note that the magnitude of the function, contrary to the real and imaginary parts, is characterized by a non vanishing average over the unit cell.

Fig. 5 illustrates the magnitude of the dimensionless effective stiffness component $|\hat{C}_{1111}^*|$ as a function of the tuning parameter λ and the dimensionless angular frequency ω^*. Here, $|\hat{C}_{1111}^*| = |\hat{C}_{1111}|/|\hat{C}_{1111}^{ref}|$, whereby $|\hat{C}_{1111}^{ref}| = 21.72$ GPa and corresponds to the effective stiffness component computed for $\lambda = 0$ and $\omega^* = 0$. The results are presented in the selected interval $\omega^* \in [0, 10 \cdot 10^3]$, since it can be observed that the effective stiffness presents a monotonic increasing behavior as a function of ω^*

and reaches a horizontal asymptote approximately for $\omega^* > 2 \cdot 10^3$. Consistently with the response of the shunted phase, the curves exhibit vertical asymptotes in correspondence of the resonance value of the tuning parameter. Additionally, horizontal asymptotes are approached for $\lambda \to \pm\infty$. Due to the isotropic properties and geometry of the cell, the effective component $\hat{C}_{1111}$ is equal to that in the ξ_2−direction. Finally, the components of the stiffness tensor $\hat{C}_{1122} = \hat{C}_{2211}$ show the same trend of $\hat{C}_{1111}$ as a function of λ and ω^*, and are thus not depicted here.

5.3. Frequency band structure of the tunable multilayered medium at the mesoscale

Once the effective properties of the microscale cell have been computed through the asymptotic homogenization procedure described in Section 5.2, at the mesoscale, the medium can be considered as a stack of two alternating homogeneous layers along $\mathbf{e}_2$: the polymeric layer and the homogenized microstructured layer, which have length equal to L_1 and L_2, respectively, along the direction perpendicular to material layering. In this scenario, the frequency band structure of the metamaterial is investigated through the technique described in Section 4. In particular, the effects of the tuning parameter λ upon metamaterial spectrum are assessed in order to control filtering properties of the hierarchical material. As mentioned in Section 4, wave propagation along the $\mathbf{e}_2$ direction is here explored, meaning that, from now on, component k_1 of the wave vector is assumed to be vanishing.

Consider first a geometrical configuration in which the two layers have the same length, i.e. $L_2/L_1 = 1$. Fig. 6 shows the behavior of the first invariant I_1^L related to longitudinal waves, as a function of the dimensionless angular frequency $\omega^* = \omega/\omega_{ref}$, again considering $\omega^* \in [0, 2 \cdot 10^7]$. Figs. 6(a) and 6(b) refer to a tuning parameter $\lambda = 0$ and to λ approaching the resonance value λ_R, respectively. Recall that, as detailed in Section 4, pass bands are detected for the first invariant I_1^L included in the range $[-2, 2]$. Accordingly, the gray regions in Fig. 6 indicate intervals of ω^* corresponding to pass bands. Conversely, the green regions, which designate the intervals for which $I_1^L \notin [-2, 2]$, define the presence of band gaps.

It is immediately evident that the ranges of ω^* in which low frequency stop bands are identified are substantially wider for $\lambda \to \lambda_R^+$ with respect to the case $\lambda = 0$. The behavior of I_1^S is not represented here, since it is conceptually analogous to that of I_1^L.

For the specific case of $\lambda = 0$, and again for a system geometry with $L_2/L_1 = 1$, Fig. 7(a) illustrates the real and the imaginary components of the eigenvalue γ, obtained by solving the standard eigenvalue problem (54) in the selected range $\omega^* \in [0, 2 \cdot 10^7]$. Black curves refer to the Floquet multiplier associated to longitudinal waves, while red curves refer to the multiplier corresponding to shear waves. It can be noted that imaginary components γ_i belong to the interval $[-1, 1]$, while real components γ_r escape from the unitary cylinder at some frequencies ω^*. This phenomenon happens in the correspondence of band gaps and can also be visualized in the top view shown in Fig. 7(b). Furthermore, the effect of viscosity is evident in Fig. 7(b), since the escapes of γ_r from the unitary circle are not straight lines, but, rather, assume a sort of bell-shape. Fig. 7(c) shows the real and the imaginary parts of the wave vector component k_2, expressed in terms of the dimensionless wave number $k_2^* = k_2 L$ (with L the total length of periodic cell $\mathcal{A}_M$), for the same dimensionless frequency range. The wave vector k_2 has been obtained through Eq. (60). Again, black and red colors refer to longitudinal and shear waves, respectively. The thin black and red curves in Fig. 7(c) represent a translation of the obtained frequency spectrum along the k_{2r}^* axis and have been inserted
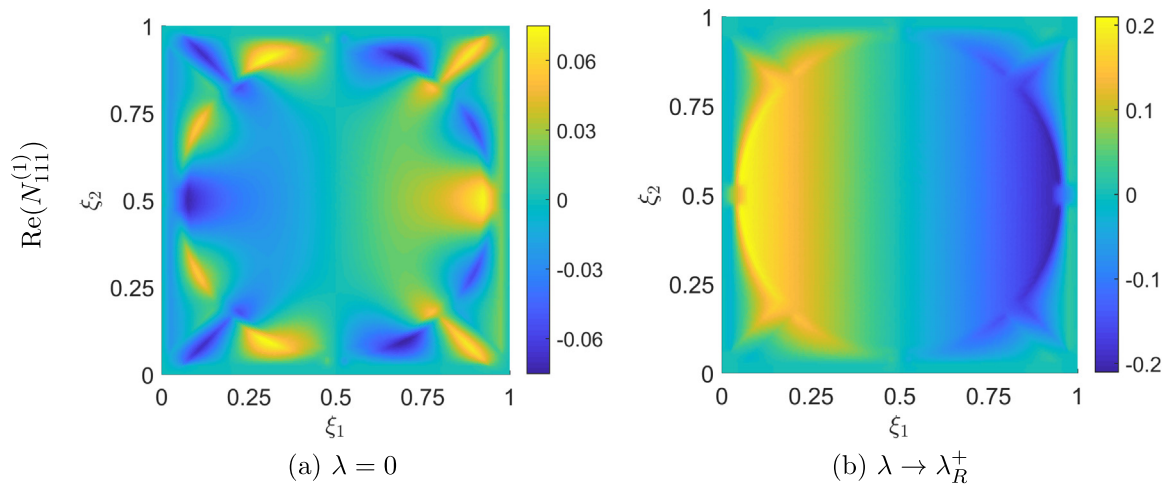
Fig. 3. Local response at the microscale. Perturbation function component $N_{111}^{(1)} = \text{Re}(N_{111}^{(1)})$ in the case of $\omega^* = 0$ for a tuning parameter (a) $\lambda = 0$; (b) $\lambda \to \lambda_R^+$.
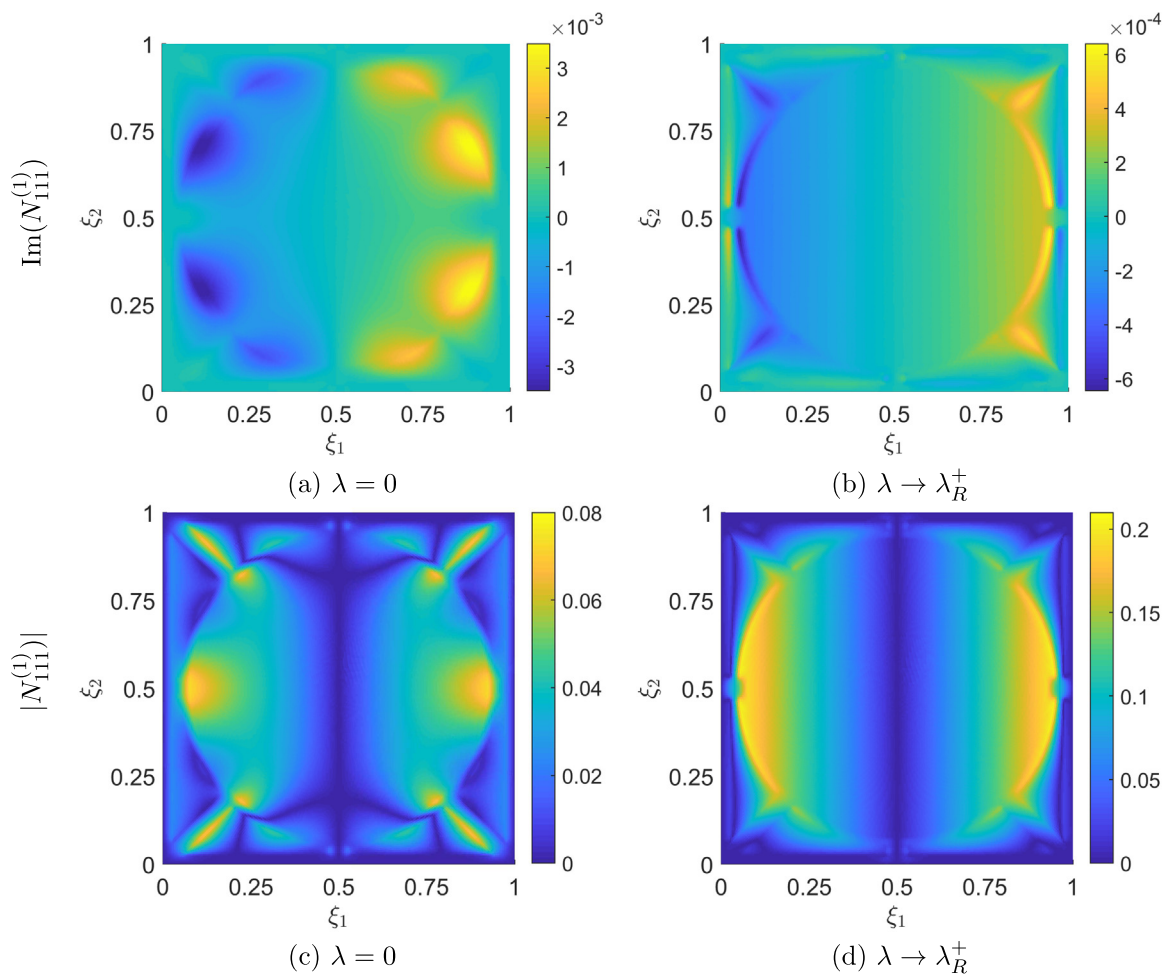

Fig. 4. Local response at the microscale. Perturbation function component $N_{111}^{(1)}$ in the case of $\omega^* = 10^4$. Imaginary part $\text{Im}(N_{111}^{(1)})$ for a tuning parameter (a) $\lambda = 0$; (b) $\lambda \to \lambda_R^+$. Magnitude $|N_{111}^{(1)}|$ for a tuning parameter (c) $\lambda = 0$; (d) $\lambda \to \lambda_R^+$.

in order to emphasize spectrum periodicity along that direction, being $k_{2r}^* \in (-\pi, \pi]$. Pass bands of propagating waves are characterized by vanishing values of k_{2i}^*, while values $k_{2i}^* \neq 0$ denote material band gaps related to spatial wave attenuation. The influence of viscosity can be further identified, by observing

that different loops in Fig. 7(c), which characterize band gaps, do not close in correspondence with $k_{2i}^* = 0$, but remain open. If the material was elastic, these loops would be contained in planes $(k_{2i}^* - \omega^*)$ characterized by a constant value of k_{2r}^* (multiple of π), but this is not the case in the presence of viscous dissipation.
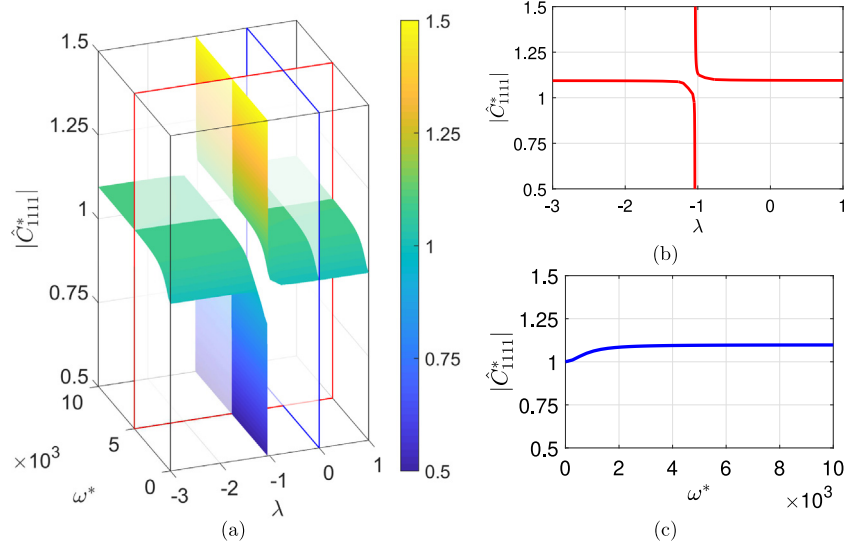
Fig. 5. Effective frequency-dependent stiffness of the microscale cell. Dimensionless magnitude of the stiffness component $|\hat{C}^*_{1111}|$ (a) as a function of the tuning parameter λ and the angular frequency ω^*; (b) as a function of λ and for $\omega^* = 5 \cdot 10^3$; (c) as a function of ω^* and for $\lambda = 0$.
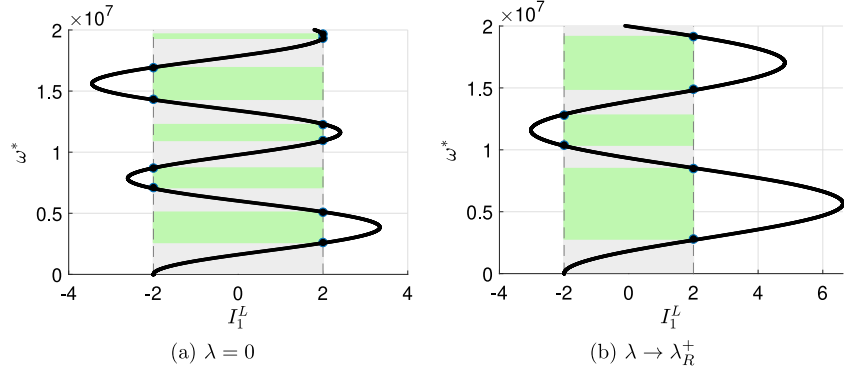
Fig. 6. Response of a system with layers of equal length ($L_2/L_1 = 1$). First invariant I_1^L associated to longitudinal waves as a function of ω^* for (a) $\lambda = 0$; (b) $\lambda \to \lambda_R^+$.

It is anticipated that this feature of the viscous response can be visualized more clearly from a two dimensional perspective, as illustrated in Figs. 8(b) and (d) and in Figs. 9(b) and (d).

The effect of the tuning parameter λ, which modifies the elastic properties of the shunting piezoelectric phase as discussed in Section 5.2, on the metamaterial frequency spectrum is demonstrated in Fig. 8. The results are again referred to a system with equal layer lengths, i.e. $L_2/L_1 = 1$. Figs. 8(a) and 8(b) show the material spectrum associated to compressional waves in the planes ($k^*_{2r} - \omega^*$) and ($k^*_{2i} - \omega^*$), respectively. Black curves represent the results for $\lambda = 0$, while gray curves correspond to branches for λ approaching the resonance value λ_R. It is evident that for $\lambda \to \lambda_R^+$ the low frequency band gaps become wider and that the corresponding central frequency increases. This confirms that triggering the shunting effect has a great impact upon metamaterial spectrum properties, particularly upon its filtering performances. Figs. 8(c) and 8(d) show, respectively, material frequency spectrum associated to shear waves in the planes ($k^*_{2r} - \omega^*$) and ($k^*_{2i} - \omega^*$) for $L_2/L_1 = 1$, for $\lambda = 0$ (blue curves) and $\lambda \to \lambda_R^+$ (cyan curves). This further demonstrates the effect of the tuning parameter in increasing the amplitude of band gaps and the value of their central frequency. In the case of shear waves, however, the tuning parameter has a lower influence on the obtained frequency spectrum than in the case of compressional waves.

Consider now the case of a material geometry for which the layers have a different relative length, with $L_2/L_1 = 10$. Figs. 9(a) and 9(b) represent the spectrum associated to longitudinal waves in the plane ($k^*_{2r} - \omega^*$) and ($k^*_{2i} - \omega^*$), respectively, for $\lambda = 0$ (black curves) and $\lambda \to \lambda_R^+$ (gray curves). Spectra related to shear waves in the planes ($k^*_{2r} - \omega^*$) and ($k^*_{2i} - \omega^*$) are plotted in Figs. 9(c) and 9(d), for $\lambda = 0$ (blue curves) and $\lambda = \lambda_R$ (cyan curves). It is confirmed that the activation of piezoelectric shunting in the tunable metamaterial opens band gaps, enhancing the filtering properties, and increases the relative central frequency. The opening of band gaps remains more substantial for longitudinal waves than for shear waves. Further, shear waves exhibit a more pronounced effect of viscosity.

The influence of the geometrical configuration on the obtained material spectrum is explored in more detail, by considering systems characterized by different relative layer lengths, which vary in the range $L_2/L_1 \in [0.1, 10]$. Figs. 10(a) and 10(b) show the dimensionless amplitude $A^* = A/\omega_{ref}$ and the dimensionless central frequency $\bar{\omega}^* = \bar{\omega}/\omega_{ref}$ of the first band gap, as a function of the ratio L_2/L_1 between the length of the microstructured layer and that of the homogeneous layer. Black and red colors indicate longitudinal and shear waves, respectively; further, continuous lines refer to $\lambda = 0$, while dashed lines to $\lambda \to \lambda_R^+$. In all the examined cases, A^* and $\bar{\omega}^*$ present a peak in correspondence with $L_2/L_1 = 1$. On the contrary, when one layer is much longer
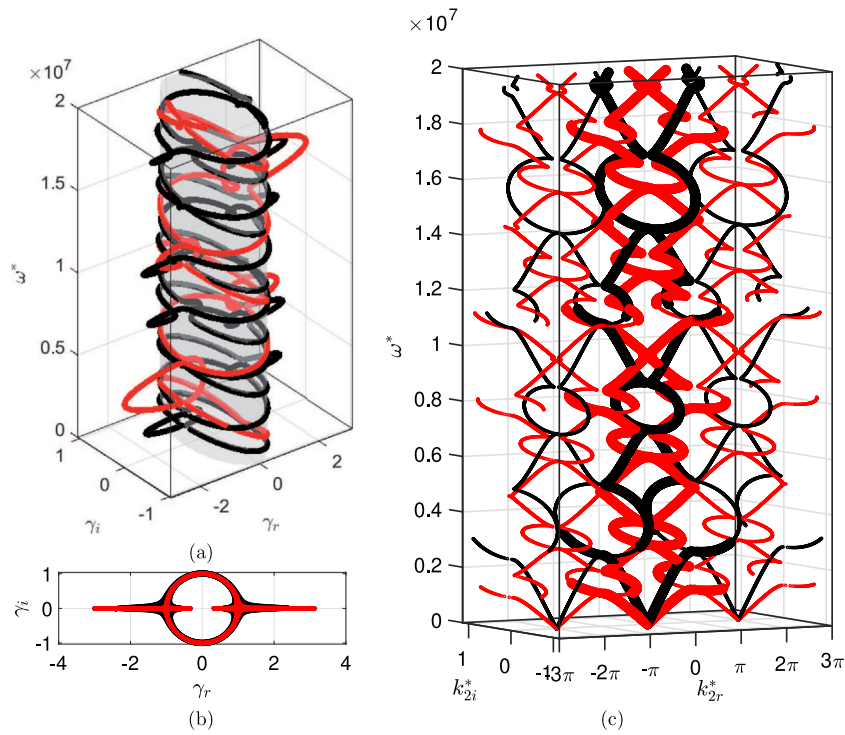
Fig. 7. Response of a system with layers of equal length ($L_2/L_1 = 1$), for a tuning parameter $\lambda = 0$. (a) Floquet multiplier components γ_r and γ_i as a function of ω^* for longitudinal waves (black curves) and shear waves (red curves). (b) 2D view of Floquet multiplier components γ_r and γ_i. (c) 3D frequency spectrum representing dimensionless components k_{2r}^* and k_{2i}^* as a function of dimensionless frequency ω^* for longitudinal waves (black curves) and shear waves (red curves).
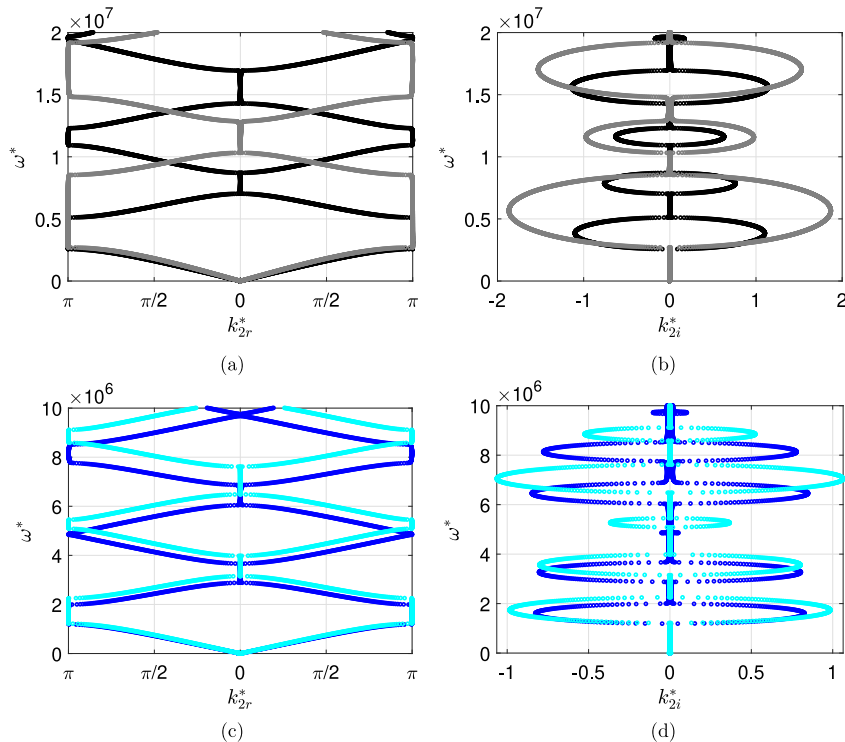
Fig. 8. Response of a system with layers of equal length ($L_2/L_1 = 1$). 2D material spectrum associated to longitudinal waves (a) in the plane ($k_{2r}^* - \omega^*$) and (b) in the plane ($k_{2i}^* - \omega^*$) for $\lambda = 0$ (black curves) and $\lambda \to \lambda_R^+$ (gray curves). 2D material spectrum associated to shear waves (c) in the plane ($k_{2r}^* - \omega^*$) and (d) ($k_{2i}^* - \omega^*$), for $\lambda = 0$ (blue curves) and $\lambda \to \lambda_R^+$ (cyan curves). The results are shown in selected frequency ranges to emphasize the tuning effect, with $\omega^* \in [0, 2 \cdot 10^7]$ for compressional waves and $\omega^* \in [0, 10^7]$ for shear waves.

or much shorter than the other, the resulting material response approximates the behavior of an elastic homogeneous medium, which does not exhibit band gaps in the frequency spectrum.

Further, for any value of L_2/L_1, it is evident that the amplitude A^* and the relative central frequency $\bar{\omega}^*$ are larger for $\lambda \to \lambda_R^+$ than for $\lambda = 0$. Additionally, it can be noted that an increase of the
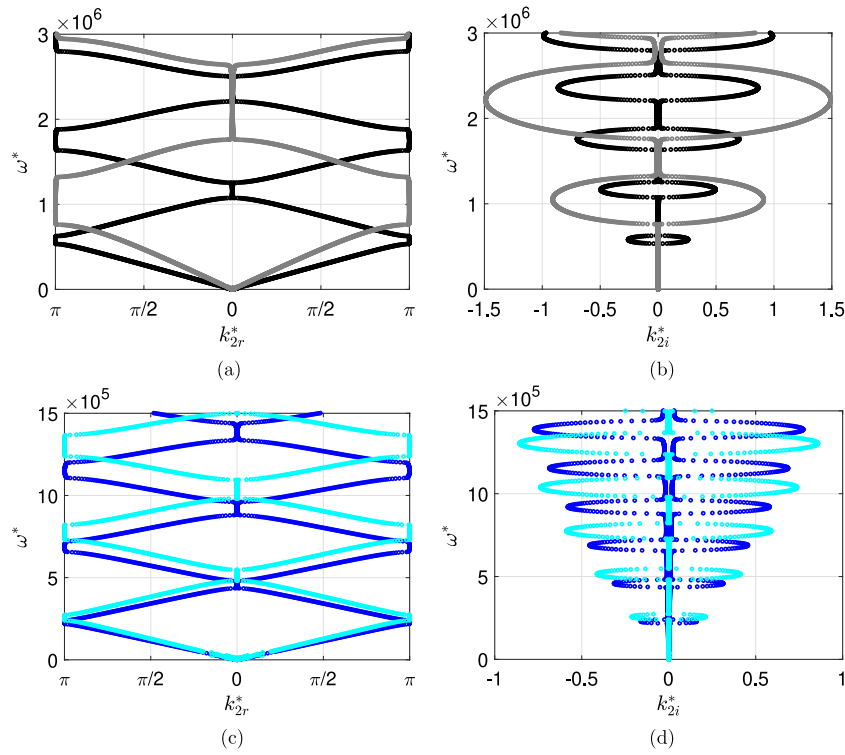
Fig. 9. Response of a system with different relative layer lengths ($L_2/L_1 = 10$). 2D material spectrum associated to longitudinal waves (a) in the plane ($k_{2r}^* - \omega^*$) and (b) in the plane ($k_{2i}^* - \omega^*$), for $\lambda = 0$ (black curves) and $\lambda \to \lambda_R^+$ (gray curves). 2D material spectrum associated to shear waves (c) in the plane ($k_{2r}^* - \omega^*$) and (d) in the plane ($k_{2i}^* - \omega^*$), for $\lambda = 0$ (blue curves) and $\lambda \to \lambda_R^+$ (cyan curves). The results are shown in selected frequency ranges to emphasize the tuning effect, with $\omega^* \in [0, 3 \cdot 10^6]$ for compressional waves and $\omega^* \in [0, 1.5 \cdot 10^6]$ for shear waves.
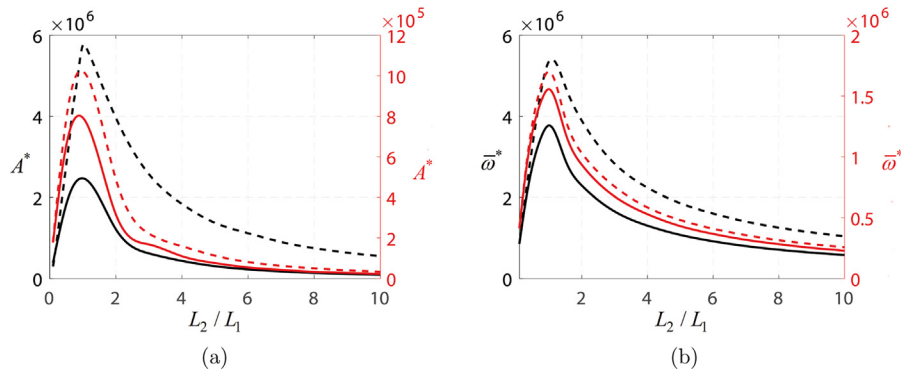

Fig. 10. Influence of relative layer length L_2/L_1 on the response of the metamaterial. (a) Dimensionless amplitude A^* of the first band gap and (b) dimensionless central frequency $\bar{\omega}^*$ of the first band gap, as a function of the ratio L_2/L_1 ratio between the thicknesses of the layers. Black curves refer to longitudinal waves, while red curves to shear waves. Continuous lines refer to $\lambda = 0$, while dashed lines to $\lambda \to \lambda_R^+$.

thickness of the microstructured layer, which thereby increases the shunting effect, results in an increase of the ratio between the band gap amplitude at $\lambda \to \lambda_R^+$ and at $\lambda = 0$. For example, taking into account compressional waves, one has $A^*(\lambda \to \lambda_R^+)/A^*(\lambda = 0) = 6.03$ for $L_2/L_1 = 10$ and $A^*(\lambda \to \lambda_R^+)/A^*(\lambda = 0) = 2.35$ for $L_2/L_1 = 1$. This feature is not immediately evident from Fig. 10(a), but is highly relevant to assess the filtering performance of the metamaterial.

Finally, the influence of the considered number of cells $\mathcal{A}_M$ of the multilayered material on the value of the transmission coefficient c_t is explored. Without loss of generality, for this purpose, a system geometry with equal layer length, i.e. $L_2/L_1 = 1$, is considered. Fig. 11 illustrates the transmission coefficient c_t for the longitudinal displacement $\hat{U}_2$ in terms of the dimensionless

frequency ω^*, for the case of a multilayered material made by one cell (black curves), five cells (gray curves), ten cells (blue curves) and twenty cells (cyan curves). The transmission coefficient is defined as $c_t = -20\log_{10}\left(\left|T_{(1,n)22}\right|\right)$, see e.g. [88,89], where $\left|T_{(1,n)22}\right|$ is the absolute value of component 22 of the transfer matrix relative to periodic cell $\mathcal{A}_M$. It is evident that, by increasing the number of periodic cells $\mathcal{A}_M$, the transmission coefficient becomes negative and with progressively larger absolute values for frequency ranges associated to the presence of material band gaps (here identified by the light gray areas), which corresponds to a closer agreement with the hypothesis underlying Floquet–Bloch theory of infinite material.
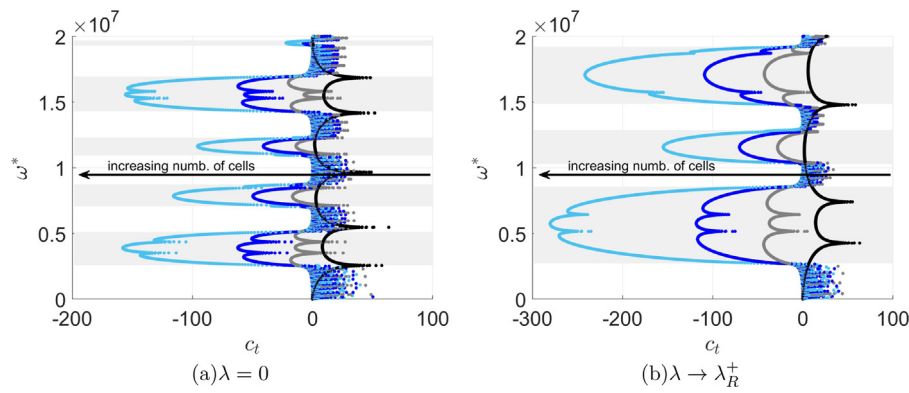
Fig. 11. Response of a system with layers of equal length ($L_2/L_1 = 1$). Transmission coefficient c_t for the longitudinal displacement $\hat{U}_2$ in terms of ω^*. The different colors refer to a number of cells $\mathcal{A}_M$ equal to one (black curves), five (gray curves), ten (blue curves), and twenty (cyan curves). Light gray areas identify frequency ranges corresponding to a band gap in the frequency spectrum for a tuning parameter (a) $\lambda = 0$, and (b) $\lambda \to \lambda_R^+$.

6. Conclusions

The present work has proposed a class of tunable nested metadevices, for which the filtering properties are controlled by means a tunable parameter, thereby enabling to obtain high performance wave propagation control. The proposed metafilter is characterized by different periodicities at different scales, and is therefore investigated within a multiscale framework. At the microscale, a square periodic cell is identified, which is made of an external rigid and heavy steel coating, connected by steel elements to an internal steel ring. A light and soft polymeric material occupies the space between the external coating and the internal ring. Inside the steel ring, a disk made of piezoelectric material is present, with a thin dielectric insulator interface separating the two phases. Piezoelectric phase is shunted by an electric external circuit characterized by a variable capacitance. The latter represents the tunable parameter able to alter the elastic constitutive properties of the piezoelectric material. Due to the periodicity of the metadevice microstructure, a two-scale first-order variational-asymptotic homogenization technique has been adopted to obtain frequency-dependent overall constitutive properties of the multiphase micro periodic cell, whereby the governing equations are written in the frequency domain by means of a bilateral Laplace transform. At the mesoscale, the metamaterial appears as a stack of two subsequent alternating layers: a polymeric homogeneous layer and the homogenized microstructured layer. These two layers are periodically repeated in plane along one direction and are infinitely extended along the perpendicular one. Material periodicity at the mesoscale allows to exploit Floquet–Bloch theory in order to investigate the dispersive free wave propagation inside the medium. Focusing on wave propagation along the direction perpendicular to material layering and to spatial damping, dispersion relation, which allows obtaining metamaterial frequency spectrum, has been determined by equating to zero the determinant of the coefficients matrix of an eigenproblem in standard form involving the transfer matrix of the periodic meso cell. Floquet multiplier plays the role of the eigenvalue of this eigenproblem, while wave polarization vector is the corresponding eigenvector.

By modifying the capacitance of the external electrical circuits, which are considered as characterized by equivalent purely capacitive admittance, the constitutive elastic properties of the piezoelectric shunting phase are consequently changed. This affects the overall constitutive behavior of the micro periodic cell that ultimately enables to obtain an adjustable frequency band structure of the metamaterial. The performance of the designed metafilter has been assessed numerically, by investigating the influence of geometrical features and of the tuning parameter on the resulting Floquet–Bloch spectrum. Triggering the shunting effect has entailed the opening of metamaterial low frequency band gaps in all the studied cases, with a consequent increase of both corresponding central frequency and amplitude. For a tuning parameter approaching the so-called resonance value, the shunted phase gets progressively stiffer, which leads to an enlargement of the corresponding low frequency band gaps, whereby the maximum filtering effect is obtained when the homogeneous polymeric layer and the microstructured layer have the same thickness along the direction perpendicular to the layering. In conclusion, the designed hierarchical metafilter has demonstrated to effectively enable passive wave propagation control in periodic materials, thereby representing a promising tool to design high performance acoustic filters.

While in this contribution a specific geometry of the multiphase microcell has been proposed, the performance of the metamaterial can be possibly improved by means of advanced parametric and topological optimization techniques [90–97]. Furthermore, more sophisticated and/or dissipative electrical circuits could be considered for the shunted phase. These interesting developments may be the topics of future research.

Declaration of competing interest

The authors declare that they have no known competing financial interests or personal relationships that could have appeared to influence the work reported in this paper.

Data availability

Data will be made available on request.

Acknowledgments

References

[1] Y. Pennec, J.O. Vasseur, B. Djafari-Rouhani, L. Dobrzyński, P.A. Deymier, Two-dimensional phononic crystals: Examples and applications, Surf. Sci. Rep. 65 (8) (2010) 229–291.

[2] M. Ouisse, M. Collet, F. Scarpa, A piezo-shunted kirigami auxetic lattice for adaptive elastic wave filtering, Smart Mater. Struct. 25 (11) (2016) 115016.

[3] A. Bacigalupo, M.L. De Bellis, G. Gnecco, Complex frequency band structure of periodic thermo-diffusive materials by Floquet–Bloch theory, Acta Mech. 230 (9) (2019) 3339–3363.

[4] A. Bacigalupo, L. Gambarotta, Chiral two-dimensional periodic blocky materials with elastic interfaces: Auxetic and acoustic properties, Extrem. Mech. Lett. (2020) 100769.

[5] L.M. Magid, Mechanical energy flow in crystal lattices, Phys. Rev. 134 (1964) A158–A162.

[6] A. Bacigalupo, M. Lepidi, Acoustic wave polarization and energy flow in periodic beam lattice materials, Int. J. Solids Struct. 147 (2018) 183–203.

[7] G. Ma, C. Fu, G. Wang, P. Del Hougne, J. Christensen, Y. Lai, P. Sheng, Polarization bandgaps and fluid-like elasticity in fully solid elastic metamaterials, Nature Commun. 7 (1) (2016) 1–8.

[8] A. Piccolroaz, A. Movchan, L. Cabras, Dispersion degeneracies and standing modes in flexural waves supported by Rayleigh beam structures, Int. J. Solids Struct. 109 (2017) 152–165.

[9] J. Park, P. Ma, Y. Kim, Design of phononic crystals for self-collimation of elastic waves using topology optimization method., Struct. Multidiscip. Optim. 51 (2015) 1199–1209.

[10] X. Han, Z. Zhang, Acoustic beam controlling in water by the design of phononic crystal, Extrem. Mech. Lett. 34 (2020) 100602.

[11] S.-H. Jo, Y. Xia, A.G. Moura, H. Yoon, Y.C. Shin, A. Erturk, B.D. Youn, Experimentally validated broadband self-collimation of elastic waves, Int. J. Mech. Sci. 192 (2021) 106131.

[12] S.-H. Jo, Y.C. Shin, W. Choi, H. Yoon, B.D. Youn, M. Kim, Double defects-induced elastic wave coupling and energy localization in a phononic crystal, Nano Convergence 8 (1) (2021) 1–13.

[13] P. Martinsson, A.B. Movchan, Vibrations of lattice structures and phononic band gaps, Quart. J. Mech. Appl. Math. 56.1 (2003) 45–64.

[14] M. Ruzzene, F. Scarpa, F. Soranna, Wave beaming effects in two-dimensional cellular structures, Smart Mater. Struct. 12 (3) (2003) 363–372.

[15] M. De Bellis, A. Bacigalupo, Auxetic behavior and acoustic properties of microstructured piezoelectric strain sensors, Smart Mater. Struct. 26 (8) (2017) 085037.

[16] H.W. Park, J.H. Oh, Study of abnormal group velocities in flexural metamaterials, Sci. Rep. 9 (2019) 13973.

[17] G. Bordiga, L. Cabras, D. Bigoni, A. Piccolroaz, Free and forced wave propagation in a Rayleigh-beam grid: Flat bands, Dirac cones, and vibration localization vs isotropization, Int. J. Solids Struct. 161 (2019) 64–81.

[18] M.L. De Bellis, A. Bacigalupo, G. Zavarise, Characterization of hybrid piezoelectric nanogenerators through asymptotic homogenization, Comput. Methods Appl. Mech. Engrg. 355 (2019) 1148–1186.

[19] L. D'Alessandro, V. Zega, R. Ardito, A. Corigliano, 3D auxetic single material periodic structure with ultra-wide tunable bandgap, Sci. Rep. 8 (1) (2018) 2262.

[20] I.V. Kamotski, V.P. Smyshlyaev, Bandgaps in two-dimensional high-contrast periodic elastic beam lattice materials, J. Mech. Phys. Solids 123 (2019) 292–304, The N.A. Fleck 60th Anniversary Volume.

[21] G. Allegri, F. Scarpa, R. Chowdhury, S. Adhikari, Wave propagation in periodically supported nanoribbons: A nonlocal elasticity approach, J. Vib. Acoust. 135 (4) (2013) 041017.

[22] F. Lemoult, N. Kaina, M. Fink, G. Lerosey, Wave propagation control at the deep subwavelength scale in metamaterials, Nat. Phys. 9 (1) (2013) 55.

[23] A. Bacigalupo, L. Gambarotta, Dispersive wave propagation in two-dimensional rigid periodic blocky materials with elastic interfaces, J. Mech. Phys. Solids 102 (2017) 165–186.

[24] A. Bacigalupo, L. Gambarotta, Wave propagation in non-centrosymmetric beam-lattices with lumped masses: Discrete and micropolar modeling, Int. J. Solids Struct. 118 (2017) 128–145.

[25] F. Dal Corso, D. Tallarico, N.V. Movchan, A.B. Movchan, D. Bigoni, Nested Bloch waves in elastic structures with configurational forces, Phil. Trans. R. Soc. A 377 (2156) (2019) 20190101.

[26] W.J. Parnell, Nonlinear pre-stress for cloaking from antiplane elastic waves, Proc. Royal Soc. A Math. Phys. Eng. Sci. 468 (2138) (2011) 563–580.

[27] D. Colquitt, M. Brun, M. Gei, A. Movchan, N. Movchan, I. Jones, Transformation elastodynamics and cloaking for flexural waves, J. Mech. Phys. Solids 72 (2014) 131–143.

[28] M. Kadic, T. Bückmann, R. Schittny, P. Gumbsch, M. Wegener, Penta-mode metamaterials with independently tailored bulk modulus and mass density, Phys. Rev. A 2 (5) (2014) 054007.

[29] L. Zigoneanu, B.I. Popa, S.A. Cummer, Three-dimensional broadband omnidirectional acoustic ground cloak, Nature Mater. 13 (4) (2014) 352.

[30] A. Darabi, A. Zareei, M. Alam, M.J. Leamy, Experimental demonstration of an ultrabroadband nonlinear cloak for flexural waves, Phys. Rev. Lett. 121 (17) (2018) 174301.

[31] D. Misseroni, A. Movchan, D. Bigoni, Omnidirectional flexural invisibility of multiple interacting voids in vibrating elastic plates, Proc. R. Soc. Lond. Ser. A Math. Phys. Eng. Sci. 475 (2019) 2229.

[32] M.-H. Lu, L. Feng, Y.-F. Chen, Phononic crystals and acoustic metamaterials, Mater. Today 12 (12) (2009) 34–42.

[33] X.N. Liu, G.K. Hu, G.L. Huang, C.T. Sun, An elastic metamaterial with simultaneously negative mass density and bulk modulus, Appl. Phys. Lett. 98 (25) (2011) 251907.

[34] X. Zhou, X. Liu, G. Hu, Elastic metamaterials with local resonances: An overview, Theor. Appl. Mech. Lett. 4 (2012) 041001.

[35] D. Bigoni, S. Guenneau, A. Movchan, M. Brun, Elastic metamaterials with inertial locally resonant structures: Application to lensing and localization, Phys. Rev. B 87 (17) (2013) 174303.

[36] A. Bacigalupo, L. Gambarotta, Simplified modelling of chiral lattice materials with local resonators, Int. J. Solids Struct. 83 (2016) 126–141.

[37] S.A. Cummer, J. Christensen, A. Alù, Controlling sound with acoustic metamaterials, Nat. Rev. Mater. 1.3 (2016) 16001.

[38] G. Ma, P. Sheng, Acoustic metamaterials: From local resonances to broad horizons, Sci. Adv. 2 (2) (2016).

[39] X. Zhou, J. Wang, R. Wang, J. Lin, Effects of relevant parameters on the bandgaps of acoustic metamaterials with multi-resonators, Appl. Phys. A 122 (2016) 427.

[40] N. Kaina, A. Causier, Y. Bourlier, M. Fink, T. Berthelot, G. Lerosey, Slow waves in locally resonant metamaterials line defect waveguides, Sci. Rep. 7 (1) (2017) 15105.

[41] M. Lepidi, A. Bacigalupo, Multi-parametric sensitivity analysis of the band structure for tetrachiral acoustic metamaterials, Int. J. Solids Struct. 136–137 (2018) 186–202.

[42] J. Liu, H. Guo, T. Wang, A review of acoustic metamaterials and phononic crystals, Crystals 10 (4) (2020) 305.

[43] R. Christensen, Theory of Viscoelasticity: An Introduction, Elsevier, 2012.

[44] L. Morini, Y. Eyzat, M. Gei, Negative refraction in quasicrystalline multilayered metamaterials, J. Mech. Phys. Solids 124 (2019) 282–298.

[45] G. Bordiga, L. Cabras, A. Piccolroaz, D. Bigoni, Prestress tuning of negative refraction and wave channeling from flexural sources, Appl. Phys. Lett. 114 (2019) 041901.

[46] A.N. Norris, A.L. Shuvalov, Elastic cloaking theory, Wave Motion 48 (2011) 525–538.

[47] D. Misseroni, D. Colquitt, A. Movchan, N. Movchan, I. Jones, Cymatics for the cloaking of flexural vibrations in a structured plate, Sci. Rep. 6 (2016) 23929.

[48] J. Park, C. Park, K. Lee, S. Lee, Acoustic superlens using membrane-based metamaterials, Appl. Phys. Lett. 106 (5) (2015) 051901.

[49] B. Brun, N. Moreau, S. Somanchi, V.H. Nguyen, K. Watanabe, T. Taniguchi, J. Charlier, C. Stampfer, B. Hackens, Imaging Dirac fermions flow through a circular Veselago lens, Phys. Rev. B 100 (2019) 041401, (R).

[50] G. Ji, J. Huber, Recent progress in acoustic metamaterials and active piezoelectric acoustic metamaterials - A review, Appl. Mater. Today 26 (2022) 101260.

[51] W. Akl, A. Baz, Analysis and experimental demonstration of an active acoustic metamaterial cell, J. Appl. Phys. 111 (2012) 044505.

[52] L. Ning, Y.-Z. Wang, Y.-S. Wang, Active control of elastic metamaterials consisting of symmetric double Helmholtz resonator cavities, Int. J. Mech. Sci. 153–154 (2019) 287–298.

[53] W. Akl, A. Baz, Active acoustic metamaterial with simultaneously programmable density and bulk modulus, J. Vib. Acoust. 135 (3) (2013) 031001.

[54] R.L. Forward, Electronic damping of vibrations in optical structures, Appl. Opt. 18 (1979) 690–697.

[55] S. Chen, Y. Fan, Q. Fu, H. Wu, Y. Jin, J. Zheng, F. Zhang, A review of tunable acoustic metamaterials, Appl. Sci. 8 (9) (2018) 1480.

[56] K. Marakakis, G.K. Tairidis, P. Koutsianitis, G.E. Stavroulakis, Shunt piezoelectric systems for noise and vibration control: A review, Front. Built Environ. 5 (2019) 64.

[57] F. Zangeneh-Nejad, R. Fleury, Active times for acoustic metamaterials, Rev. Phys. 4 (2019) 100031.

[58] E. Sanchez Palencia, Non-Homogeneous Media and Vibration Theory, Springer, 1980.

[59] N.S. Bakhvalov, G.P. Panasenko, Homogenization: Averaging Processes in Periodic Media, Kluwer Academic Publishers, Dordrecht-Boston-London, 1984.

[60] I. Temizer, On the asymptotic expansion treatment of two-scale finite thermoelasticity, Internat. J. Engrg. Sci. 53 (2012) 74–84.

[61] G. Chatzigeorgiou, N. Charalambakis, Y. Chemisky, F. Meraghni, Periodic homogenization for fully coupled thermomechanical modeling of dissipative generalized standard materials, Int. J. Plast. 81 (2016) 18–39.

[62] C. Vega, J. Pina, E. Bosco, E. Flores, C. Guzman, S. Yanez, Thermo-mechanical analysis of wood through an asymptotic homogenisation approach, Constr. Build. Mater. 315 (2022) 125617.

[63] A. Bacigalupo, L. Morini, A. Piccolroaz, Multiscale asymptotic homogenization analysis of thermo-diffusive composite materials, Int. J. Solids Struct. 85 (2016) 15–33.

[64] F. Fantoni, A. Bacigalupo, Wave propagation modeling in periodic elasto-thermo-diffusive materials via multifield asymptotic homogenization, Int. J. Solids Struct. 196–197 (2020) 99–128.

[65] F. Fantoni, A. Bacigalupo, M. Paggi, Multi-field asymptotic homogenization of thermo-piezoelectric materials with periodic microstructure, Int. J. Solids Struct. 120 (2017) 31–56.

[66] F. Fantoni, A. Bacigalupo, M. Paggi, Design of thermo-piezoelectric microstructured bending actuators via multi-field asymptotic homogenization, Int. J. Mech. Sci. 146 (2018) 319–336.

[67] E. Rohan, V. Lukeš, Homogenization of the fluid-saturated piezoelectric porous media, Int. J. Solids Struct. 147 (2018) 110–125.

[68] E. Bosco, R. Peerlings, M. Geers, Hygro-mechanical properties of paper fibrous networks through asymptotic homogenization and comparison with idealized models, Mech. Mater. 108 (2017) 11–20.

[69] E. Bosco, R. Peerlings, M. Geers, Asymptotic homogenization of hygro-thermo-mechanical properties of fibrous networks, Int. J. Solids Struct. 115–116 (2017) 180–189.

[70] M. Livani, E. Bosco, A. Suiker, Influence of morphology on the effective hygro-elastic properties of softwood (spruce) and hardwood (balsa), Arch. Appl. Mech. 91 (2021) 4141–4162.

[71] E. Bosco, R. Claessens, A. Suiker, Multi-scale prediction of chemo-mechanical properties of concrete materials through asymptotic homogenization, Cem. Concr. Res. 128 (2020) 105929.

[72] R.E.A.C. Paley, N. Wiener, Fourier Transforms in the Complex Domain, Vol. 19, American Mathematical Soc., 1934.

[73] G. Floquet, Sur les équations différentielles linéaires à coefficients périodiques, Ann. Sci. L'école Normale Supérieure 12 (1883)) 47–88.

[74] M. Faulkner, D. Hong, Free vibrations of a mono-coupled periodic system, J. Sound Vib. 99 (1) (1985) 29–42.

[75] G.S. Gupta, Natural flexural waves and the normal modes of periodically-supported beams and plates, J. Sound Vib. 13 (1) (1970) 89–101.

[76] A. Bacigalupo, M.L. De Bellis, D. Misseroni, Design of tunable acoustic metamaterials with periodic piezoelectric microstructure, Extrem. Mech. Lett. 40 (2020) 100977.

[77] R. Toupin, Stress tensors in elastic dielectrics, Arch. Ration. Mech. Anal. 5 (1) (1960) 440–452.

[78] J. Westra, C. Verhoeven, A. Van Roermund, Oscillators and Oscillator Systems, Springer, 2000.

[79] V.P. Smyshlyaev, K.D. Cherednichenko, On rigorous derivation of strain gradient effects in the overall behaviour of periodic heterogeneous media, J. Mech. Phys. Solids 48 (2000) 1325–1357.

[80] A. Bacigalupo, Second-order homogenization of periodic materials based on asymptotic approximation of the strain energy: Formulation and validity limits, Meccanica 49 (2014) 1407–1425.

[81] A. Bacigalupo, L. Gambarotta, Multi-scale strain-localization analysis of a layered strip with debonding interfaces, Int. J. Solids Struct. 50 (2013) 2061–2077.

[82] G.B. Arfken, H.J. Weber, Mathematical Methods for Physicists, fifth ed., Elsevier Academic Press, San Diego, 2005.

[83] R. Broucke, VI Arnold, mathematical methods of classical mechanics (book review), Celestial Mech. 28 (1982) 345.

[84] D. Hennig, G.P. Tsironis, Wave transmission in nonlinear lattices, Phys. Rep. 307 (5–6) (1999) 333–432.

[85] J.C. Bronski, Z. Rapti, Modulational instability for nonlinear Schrödinger equations with a periodic potential, Dyn. Partial Differ. Equ. 2 (4) (2005) 335–355.

[86] G. Caviglia, A. Morro, Inhomogeneous Waves in Solids and Fluids, Vol. 7, World Scientific, 1992.

[87] J. Carcione, Wave Fields in Real Media: Wave Propagation in Anisotropic, Anelastic, Porous and Electromagnetic Media, Elsevier, 2007.

[88] B. Li, S. Alamri, K. Tan, A diatomic elastic metamaterial for tunable asymmetric wave transmission in multiple frequency bands, Sci. Rep. 7 (1) (2017) 1–14.

[89] M. Choi, M. Oh, B. Koo, S. Cho, Optimal design of lattice structures for controllable extremal band gaps, Sci. Rep. 9 (1) (2019) 1–13.

[90] A. Diaz, A. Haddow, L. Ma, Design of band-gap grid structures, Struct. Multidiscip. Optim. 29 (6) (2005) 418–431.

[91] A. Bacigalupo, M. Lepidi, G. Gnecco, L. Gambarotta, Optimal design of auxetic hexachiral metamaterials with local resonators, Smart Mater. Struct. 25 (5) (2016) 054009.

[92] M. Ranjbar, L. Boldrin, F. Scarpa, S. Neild, S. Patsias, Vibroacoustic optimization of anti-tetrachiral and auxetic hexagonal sandwich panels with gradient geometry, Smart Mater. Struct. 25 (5) (2016) 054012.

[93] A. Bacigalupo, G. Gnecco, M. Lepidi, L. Gambarotta, Machine-learning techniques for the optimal design of acoustic metamaterials, J. Optim. Theory Appl. 187 (3) (2020) 630–653.

[94] M. Bruggi, A. Corigliano, Optimal 2D auxetic micro-structures with band gap, Meccanica 54 (13) (2019) 2001–2027.

[95] M. Choi, M. Oh, B. Koo, S. Cho, Optimal design of lattice structures for controllable extremal band gaps, Sci. Rep. 9 (1) (2019) 1–13.

[96] D. Kumar, Z. Wang, L.H. Poh, S.T. Quek, Isogeometric shape optimization of smoothed petal auxetics with prescribed nonlinear deformation, Comput. Methods Appl. Mech. Engrg. 356 (2019) 16–43.

[97] J. Rong, W. Ye, Topology optimization design scheme for broadband non-resonant hyperbolic elastic metamaterials, Comput. Methods Appl. Mech. Engrg. 344 (2019) 819–836.